DNA-driven condensation assembles the meiotic DNA break machinery

https://doi.org/10.1038/s41586-021-03374-w

Received: 15 May 2020

Accepted: 18 February 2021

Published online: 17 March 2021

Check for updates

Corentin Claeys Bouuaert[1,2]✉, Stephen Pu[1], Juncheng Wang[3], Cédric Oger[2], Dima Daccache[2], Wei Xie[3], Dinshaw J. Patel[3] & Scott Keeney[1]✉

The accurate segregation of chromosomes during meiosis—which is critical for genome stability across sexual cycles—relies on homologous recombination initiated by DNA double-strand breaks (DSBs) made by the Spo11 protein[1,2]. The formation of DSBs is regulated and tied to the elaboration of large-scale chromosome structures[3–5], but the protein assemblies that execute and control DNA breakage are poorly understood. Here we address this through the molecular characterization of *Saccharomyces cerevisiae* RMM (Rec114, Mei4 and Mer2) proteins—essential, conserved components of the DSB machinery[2]. Each subcomplex of Rec114–Mei4 (a 2:1 heterotrimer) or Mer2 (a coiled-coil-containing homotetramer) is monodispersed in solution, but they independently condense with DNA into reversible nucleoprotein clusters that share properties with phase-separated systems. Multivalent interactions drive this condensation. Mutations that weaken protein–DNA interactions strongly disrupt both condensate formation and DSBs in vivo, and thus these processes are highly correlated. In vitro, condensates fuse into mixed RMM clusters that further recruit Spo11 complexes. Our data show how the DSB machinery self-assembles on chromosome axes to create centres of DSB activity. We propose that multilayered control of Spo11 arises from the recruitment of regulatory components and modulation of the biophysical properties of the condensates.

In *S. cerevisiae*, the formation of DSBs involves the coordinated action of ten proteins in three subgroups[2]. Spo11, Rec102, Rec104 and Ski8 form the DSB enzyme ('core complex'), which is related to archaeal topoisomerases[6–10]; the MRX (Mre11, Rad50 and Xrs2) complex is also important for the processing of DSBs[2]; and the third subgroup comprises the RMM proteins, which have been grouped together on the basis of yeast-two-hybrid (Y2H) interactions, coimmunoprecipitation, and colocalization and interdependencies of their foci[11–14].

RMM proteins lie at the crossroads between DSB formation and chromosome organization: they associate with chromatin early in meiotic prophase and form overlapping, interdependent foci along chromosome axes[11,12,15,16]. They interact with other components of the DSB machinery and the hotspot-targeting protein Spp1, thereby connecting chromosome axes with sites of DNA cleavage[12,17–19]. RMM proteins are conserved, albeit with high sequence divergence[20–24], but their functions and biochemical properties remain unclear (Supplementary Discussion 1).

Heterotrimeric Rec114–Mei4 complexes

Because functional relationships between Rec114, Mei4 and Mer2 are well known[11,12,17] and have been confirmed in other species[14,21,23,25], we sought to purify a tripartite complex. However, whereas Mer2 alone and a Rec114–Mei4 complex were readily purified, we could not obtain a stable RMM complex (Extended Data Fig. 1a, b).

Much of Rec114 is predicted to be disordered (Fig. 1a, top). The N-terminal region contains six signature sequence motifs (SSMs), with a seventh located near the C terminus[12,23,26]. The N-terminal SSMs of mouse REC114 form a pleckstrin homology (PH)-like fold[25,27]. Mei4 is mostly ordered (Fig. 1a, bottom), with six SSMs[26].

Purified Rec114–Mei4 complexes had molar masses of 180 and 114 kDa (tagged and untagged, respectively) on size-exclusion chromatography with multi-angle light scattering (SEC–MALS) (Fig. 1b, c). These results, plus the intensities of Coomassie-stained bands and an observed 2:1 ratio of mass spectrometry spectral counts (Extended Data Fig. 1c), suggested a stoichiometry of two Rec114 subunits and one Mei4 subunit (expected 200 and 146 kDa for tagged and untagged, respectively).

We delineated the molecular arrangement within the complexes by crosslinking plus mass spectrometry (XL–MS), and identified 258 distinct pairs of crosslinked lysines (Fig. 1d, Supplementary Table 1). The C terminus of Rec114 crosslinked extensively to the N terminus of Mei4 (pink lines), implying that these are the primary interaction regions. Four intermolecular self-links (crosslinking of two identical lysines) occurred near the C-terminal end of Rec114 (black loops in Fig. 1d), supporting the 2:1 stoichiometry and suggesting that this domain homo-dimerizes (Fig. 1e).

[1]Molecular Biology Program, Memorial Sloan Kettering Cancer Center and Howard Hughes Medical Institute, New York, New York, USA. [2]Louvain Institute of Biomolecular Science and Technology, Université Catholique de Louvain, Louvain-La-Neuve, Belgium. [3]Structural Biology Program, Memorial Sloan Kettering Cancer Center, New York, New York, USA.
✉e-mail: corentin.claeys@uclouvain.be; s-keeney@ski.mskcc.org

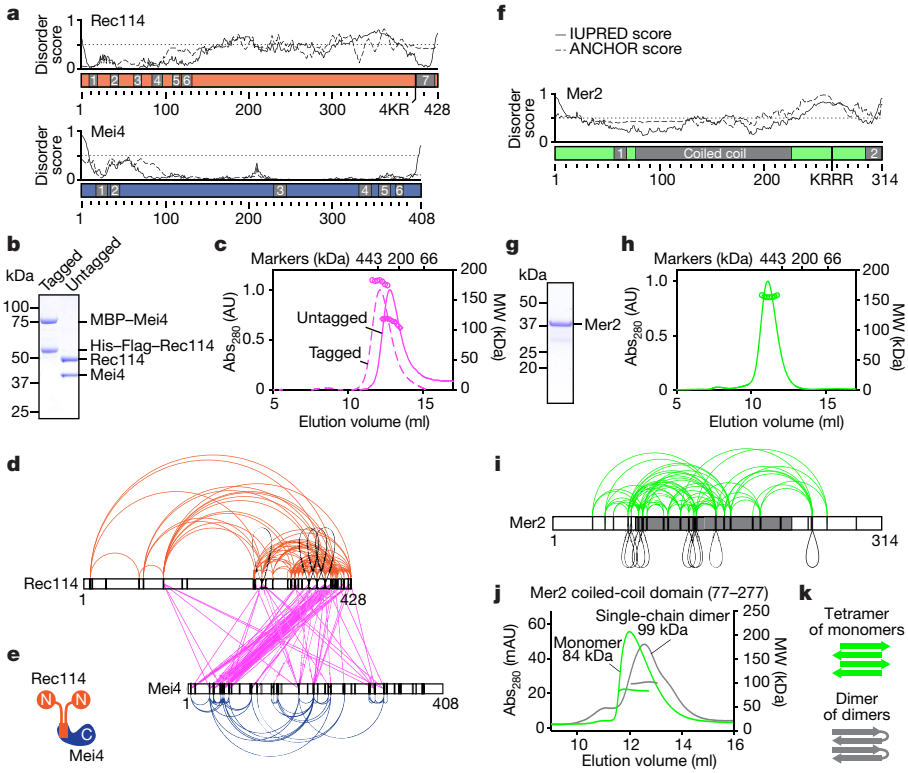

Fig. 1 | Purification and subunit arrangement of the *S. cerevisiae* RMM proteins. a, Prediction of protein disorder (IUPRED server[42]). The ANCHOR score predicts the transition from unstructured to structured depending on a binding partner. Previously identified SSMs are shown[23,26]. **b**, SDS–PAGE of purified tagged and untagged Rec114–Mei4 complexes (4 µg was loaded). **c**, SEC–MALS analysis of tagged and untagged Rec114–Mei4. The traces show ultraviolet absorbance (Abs_{280}) and circles are molar mass measurements across the peak. Elution positions of protein standards are marked (top). **d**, XL–MS analysis of Rec114–Mei4 (4,812 crosslinked peptides, 258 distinct crosslinked pairs of lysines). Black loops, intermolecular self-links; black vertical lines, lysines. **e**, Cartoon of the Rec114–Mei4 complex. **f**, Protein disorder prediction for Mer2. The predicted coiled coil and previously identified SSMs are shown[23,26]. **g**, SDS–PAGE of purified Mer2 (4 µg was loaded). **h**, SEC–MALS analysis of Mer2 as in **c**. **i**, XL–MS analysis of Mer2 as in **d** (487 crosslinked peptides, 89 distinct crosslinked pairs of lysines). **j**, SEC–MALS analysis of the coiled-coil domain of Mer2 and a single-chain dimer variant of the coiled-coil domain. A tetramer of monomers and a dimer of single-chain dimers both have an expected molecular weight (MW) of 70 kDa. The difference between the profiles of the monomer and single-chain dimer can be explained by reduced degrees of freedom (tension) in the single-chain dimer and heterogeneity. **k**, Interpretive cartoon of the molecular arrangement of the coiled-coil domain of Mer2. For gel source data, see Supplementary Fig. 1.

Truncated proteins that retained SSM7 of Rec114 and SSMs 1 and 2 of Mei4 (Rec114(375–428) and Mei4(1–43)) formed a 2:1 complex (Extended Data Fig. 1d–h). Dimerization of Rec114 C-terminal fragments did not require Mei4 (Extended Data Fig. 1h). Mutation of a conserved Rec114 residue (F411A) abolished dimerization, which disrupted the interaction with Mei4 similarly to an equivalent mutation in the *Schizosaccharomyces pombe* Rec114 orthologue Rec7[13] (Extended Data Fig. 1i–k). Rec114(F411A) was expressed at normal levels in vivo, but it eliminated Rec114 foci and DSBs, leading to spore death (Extended Data Fig. 1l–o).

A homotetrameric Mer2 α-helical bundle

Mer2 has a predicted coiled coil and two SSMs[23,28], with a disordered region between the coiled coil and SSM2 (Fig. 1f). Untagged Mer2 was 156 kDa by SEC–MALS, consistent with a tetramer (143 kDa) (Fig. 1g, h), but the elution volume matched that of a considerably larger complex, suggesting an elongated shape (see marker positions in Fig. 1h).

XL–MS revealed nine intermolecular self-links (Fig. 1i). Self-links occurred along the coiled coil, consistent with parallel α-helices, but this domain also incurred long-range crosslinks. If the coiled coil forms uninterrupted helices, crosslinks further than about 18 amino acids cannot be explained by intramolecular events or by intermolecular events within a parallel coiled coil. Therefore, it is likely that there are both parallel and antiparallel helices.

To address this, we first observed that the coiled-coil domain alone (residues 77–227) was still tetrameric (Fig. 1j). Next, we engineered a single-chain dimer with two copies of the coiled-coil domain separated by a 19 amino-acid linker, which is too short for a parallel intramolecular coiled coil. This assembled a similarly sized complex to the monomeric construct (99 versus 84 kDa), consistent with two single-chain dimers, each folded in antiparallel (Fig. 1j, k). Alternative scenarios predict an artificially elongated single-chain dimer that would lead to faster elution on size exclusion, which was not observed. A plausible configuration is thus a homotetrameric α-helical bundle with two pairs of parallel helices arranged in antiparallel fashion (Fig. 1k).

DNA-driven condensation

Rec114, Mei4 and Mer2 orthologues in yeasts and mice form chromatin-associated foci[11,12,15,16,25,26,29,30], but the physical nature of these foci is unclear. Moreover, the relationships between these structures, DSB formation, and the biochemical properties of Rec114, Mei4 and Mer2 are unknown.

In electrophoretic mobility shift assays, Rec114–Mei4 and Mer2 bound to 20-, 40-, and 80-bp substrates, with affinity increasing with DNA length (Fig. 2a, b, Extended Data Fig. 2a, b). Preference for longer substrates was confirmed in competition assays (Extended Data Fig. 2c, d). Protein titrations yielded well-shifts with no discrete bands and switch-like transitions from no binding to complete binding within

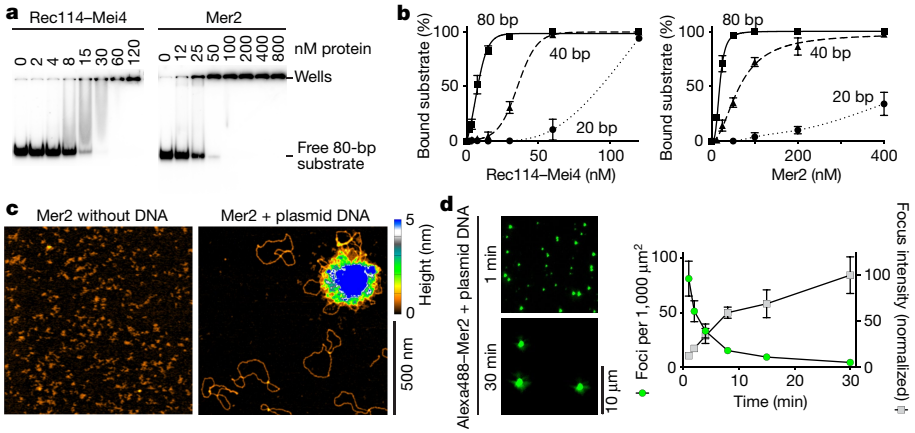

Fig. 2 | Rec114–Mei4 and Mer2 form condensates on DNA. a, Gel-shift analysis of Rec114–Mei4 and Mer2 binding to 80-bp DNA substrates (Extended Data Fig. 2a, b). **b**, Quantification of gel-shift analyses with 20-, 40- or 80-bp substrates. Error bars, ranges from two independent experiments; lines are sigmoidal curves fit to the data, except for the 20-bp substrate (smooth spline fits). Apparent affinities of Rec114–Mei4 are: 6 ± 1.4 nM (80 bp, mean ± range); 35 ± 1.3 nM (40 bp); approximately 80 nM (20 bp). Apparent affinities of Mer2 are: 19 ± 1.5 nM (80 bp); 64 ± 15 nM (40 bp); more than 400 nM (20 bp). Here and elsewhere, concentrations for Rec114–Mei4 refer to the trimeric complex, but for Mer2 they refer to the monomer. Therefore, the complexes have comparable affinities for DNA if the quaternary units (trimers and tetramers, respectively) are considered. **c**, AFM imaging of 50 nM Mer2 in the absence (left) or presence (right) of 1 nM plasmid DNA (pUC19). **d**, Time course of the assembly of Mer2 foci in the presence of plasmid DNA. The *x*-axis indicates the time in solution before plating, upon which DNA is immobilized to the glass slide while soluble protein is still free to diffuse. Focus numbers and average focus intensity (normalized to the mean at 30 min) are shown. Data shown as mean ± s.d. from 8–10 fields of view (see Source Data for exact *n* values). For gel source data, see Supplementary Fig. 1.

narrow (two- to fourfold) ranges, suggesting cooperative assembly of higher-order structures (Fig. 2a, b, Extended Data Fig. 2a, b).

To visualize DNA-bound particles directly, we used atomic force microscopy (AFM). Rec114–Mei4 and Mer2 formed small, relatively homogeneous particles on the mica surface in the absence of DNA, but plasmid DNA caused Rec114–Mei4 and Mer2 to assemble large protein clusters with emanating DNA loops (Fig. 2c, Extended Data Fig. 2g). Most plasmid molecules remained unbound and the surface was devoid of free protein particles, showing that clustering is extremely cooperative. From the sizes (approximately 0.2 μm diameter for Rec114–Mei4 and approximately 0.4 μm for Mer2), the clusters must contain many hundreds of proteins.

Rec114–Mei4 complexes with mScarlet fused to the Rec114 N terminus yielded bright epifluorescent foci in the presence of DNA, independent of Mg^{2+} (Extended Data Fig. 3a). Enhanced green fluorescent protein (eGFP)-tagged Mer2 complexes also produced DNA-dependent foci in the presence of Mg^{2+}, but gave only a diffuse fluorescence signal without Mg^{2+} (Extended Data Figs. 2e, f, 3b).

Properties of nucleoprotein condensates

Rec114–Mei4 and Mer2 nucleoprotein clusters resemble condensates that form intracellular membrane-less compartments and control transcription, signal transduction, stress responses, and other processes[31–36]. Biomolecular phase separation is often driven by cumulative weak interactions between multivalent components[31,35,36]. These condensates share biophysical properties: they tend to be reversible, are promoted by molecular crowding, can fuse, and may undergo sol-gel transitions over time.

We used fluorophore-conjugated complexes to investigate whether Rec114–Mei4 and Mer2 condensates display behaviours typical of phase-separated systems (Extended Data Fig. 3c–f). The molecular crowding agent polyethylene glycol (5% PEG-8000) markedly increased condensate intensity for both Rec114–Mei4 and Mer2 (Extended Data Fig. 3g, h). Protein titrations revealed complex, sometimes counterintuitive, behaviours, including a decrease in focus numbers with increasing protein concentrations. These behaviours are likely to reflect balances between nucleation, growth, and collapse of the condensates (legend of Extended Data Fig. 3g, h).

Condensation was inhibited by high salt levels, suggesting that it depends on electrostatic interactions (Extended Data Fig. 4c, e). Competition experiments revealed preferential incorporation of larger DNA molecules, consistent with multivalency of the substrate driving condensation (Extended Data Fig. 4g, h).

Pre-assembled condensates were almost completely dissolved when challenged with DNase I or 500 mM NaCl in the absence of PEG, showing that they are reversible (Extended Data Fig. 4a, b). However, in the presence of PEG, about half of the condensate-associated Rec114–Mei4 fluorescence signal resisted challenge. Reversibility of Rec114–Mei4 condensates decreased over time, accentuated by molecular crowding (Extended Data Fig. 4d). After a short assembly time, Mer2 condensates were unable to resist dissolution whether PEG was present or not, but longer incubation times with PEG also allowed Mer2 form resistant foci (Extended Data Fig. 4b, f). These results suggest that condensates of Rec114–Mei4 and, to a lesser extent, Mer2 may spontaneously mature into irreversible, perhaps gel-like, structures, as has previously been observed for other systems[35,37–39].

Several scenarios might account for condensate assembly, differing as to whether growth results principally from fusion of existing condensates or from incorporation of soluble protein that diffuses in and out of condensates (Extended Data Fig. 5a). To distinguish between these possibilities, we immobilized DNA at varying time points by spreading assembly reactions on glass slides. Plating should prevent focus fusion, but not exchange of condensates with soluble protein pools. Images were captured at a late time point (>1 h after spreading), so the time variable is the period for which the DNA is free in solution before constraint. If foci grow by addition from soluble protein pools, DNA immobilization should have no effect and all reactions should be identical. By contrast, if fusion drives growth, focus numbers should decrease over time while their intensities increase. The latter outcome was observed for both Rec114–Mei4 and Mer2 (Fig. 2d, Extended Data Fig. 5b). Moreover, no fluorescence recovery was seen after photobleaching of immobilized foci (Extended Data Fig. 5c). These findings establish that fusion can occur. However, they do not exclude the possibility that exchange with soluble pools is important under other conditions, including in vivo (Supplementary Discussion 2).

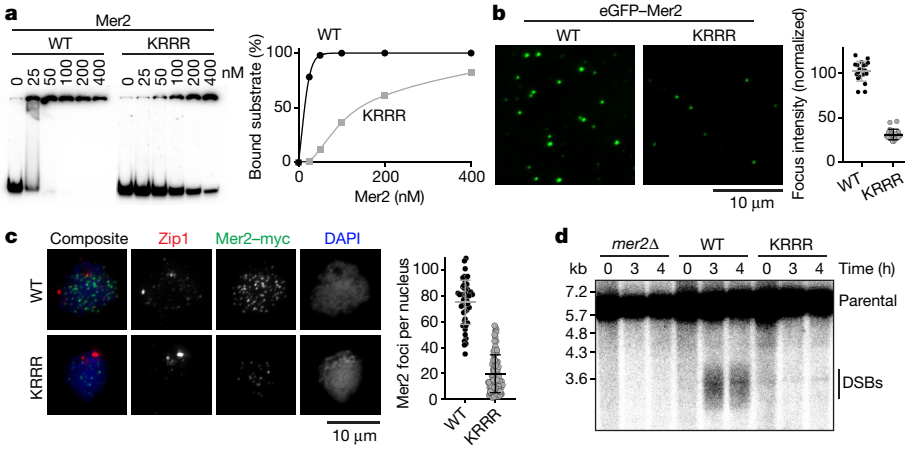

Fig. 3 | DNA binding by Mer2 is important for macromolecular condensation in vitro and in vivo and for Spo11-induced break formation. **a**, Gel-shift assay of wild-type (WT) and mutant (KRRR) Mer2 complexes binding to an 80-bp DNA substrate. The Mer2(KRRR) mutant has residues K265, R266, R267, and R268 mutated to alanine. Lines on the graph are a sigmoidal curve (wild type) and a smooth spline (KRRR) fit to the data. **b**, Effect of the Mer2(KRRR) mutation on condensation in vitro. Reactions included 5% PEG. Each point is the average of the intensities of foci in a field of view, normalized to the overall mean for the wild type. Data shown as mean ± s.d. (n = 20 fields of view). **c**, Immunofluorescence on meiotic chromosome spreads for myc-tagged Mer2. The number of foci per leptotene or early zygotene cell is plotted. Data shown as mean ± s.d. (n = 48 and 95 cells for wild type and Mer2(KRRR), respectively). **d**, Southern blot analysis of meiotic DSB formation at the *CCT6* hotspot in wild-type and *mer2* mutant strains. For gel source data, see Supplementary Fig. 1.

DNA binding and RMM function

The Rec114 C-terminal domain is necessary and sufficient for DNA binding (Extended Data Fig. 6a). Alanine substitution of four basic residues in this domain yielded a Rec114–Mei4 complex (4KR) with reduced DNA binding (Extended Data Fig. 6b). Similarly, alanine substitutions in a conserved basic patch towards the C terminus of Mer2 (KRRR) yielded a mutant that was defective in DNA binding (Fig. 3a, Extended Data Fig. 6c). As expected if multivalent protein–DNA interactions contribute to condensation, both the Rec114(4KR) and Mer2(KRRR) mutant proteins showed strongly reduced focus formation in vitro (Fig. 3b, Extended Data Fig. 6d). However, fluorescently tagged Mer2(KRRR) was incorporated into pre-assembled Mer2 condensates as efficiently as wild-type Mer2 (Extended Data Fig. 6e), indicating that the protein–protein interactions that are important for condensation are retained in the mutant.

In vivo, the mutant proteins formed many fewer foci than did the wild type upon immunofluorescent staining of chromosome spreads[11,12,15] (Fig. 3c, Extended Data Fig. 6f). This could not be attributed to protein destabilization because the immunoblotting signal was not reduced compared to that of the wild type (Extended Data Fig. 6g) and purified recombinant proteins did not show increased sensitivity to digestion with trypsin (Extended Data Fig. 6h). In fact, the Mer2(KRRR) mutant protein accumulated and persisted for longer during meiosis than the wild type (Extended Data Fig. 6i). The Mer2(KRRR) protein also had higher electrophoretic mobility than the wild type, probably because it did not become phosphorylated. It therefore appears that DNA binding is a prerequisite for Mer2 phosphorylation, which is known to promote turnover of the protein[15].

Both mutations also conferred defects in meiotic DSB formation when assayed locally by Southern blotting at a DSB hotspot (Fig. 3d, Extended Data Fig. 6j) or globally by quantification of Spo11–oligonucleotide complexes (Extended Data Fig. 6k). These DSB defects caused low spore viability (Extended Data Fig. 6l). In conclusion, the DNA-binding activities of Rec114–Mei4 and Mer2 are essential for DNA-driven condensation in vitro and in vivo and for their DSB-promoting activity, suggesting in turn that condensation itself is important for these proteins' biological functions.

Comingled RMM nucleoprotein condensates

In vivo, Rec114, Mei4 and Mer2 form partially overlapping foci[11,12] and yield coincident chromatin immunoprecipitation signals[16]. We therefore tested whether they function together as joint condensates by mixing fluorescent Rec114–Mei4 and Mer2 either before or after DNA-driven condensation (Fig. 4a, b). Premixing of the proteins led to joint foci with essentially perfect overlap (Fig. 4a). Colocalization was evident even with a large excess of DNA, so joint foci were not the result of fortuitous overlap of independent assemblies on limiting numbers of substrate molecules (Extended Data Fig. 7a, b).

Next, we investigated whether preassembled Rec114–Mei4 and Mer2 condensates can mingle. We found no overlap between Rec114–Mei4 and Mer2 foci when preformed nucleoprotein condensates were mixed and then immediately plated (Fig. 4b, top). By contrast, when the mixtures were incubated for 20 min before plating, all of the Mer2 condensates overlapped with a Rec114–Mei4 focus (Fig. 4b, bottom). The lack of overlap in samples that were plated immediately rules out the possibility of the joint foci arising via a pool of soluble protein under these conditions, so we infer that existing condensates can fuse.

To further test this inference, we performed a time-course experiment with different concentrations of Rec114–Mei4 (17 and 35 nM) (Fig. 4c). As shown above, the lower concentration yielded more foci (Extended Data Fig. 3g). If the likelihood of cluster fusion reflects contact probability, the rate at which joint foci form would be expected to be higher with the lower concentration of Rec114–Mei4. This was indeed the case: the halftime for detecting joint foci was 2.0 ± 0.3 min for 17 nM compared with 3.3 ± 0.6 min for 35 nM (Fig. 4c, right).

We also tested whether soluble protein can be recruited into condensates. Here, Rec114–Mei4 or Mer2 condensates were assembled, and then the other protein was added in solution and the mixtures were immediately plated to prevent subsequent fusion. Preassembled Rec114–Mei4 foci incorporated Mer2 and vice versa (Extended Data Fig. 7c), showing that condensates provide nucleation sites for the partner complexes.

Interaction of Mer2 and Rec114–Mei4 complexes within nucleoprotein condensates might account for their interactions in immunoprecipitation and Y2H experiments[11–14,17], even though they do not form a stable tripartite complex (Extended Data Fig. 1a, b). We observed

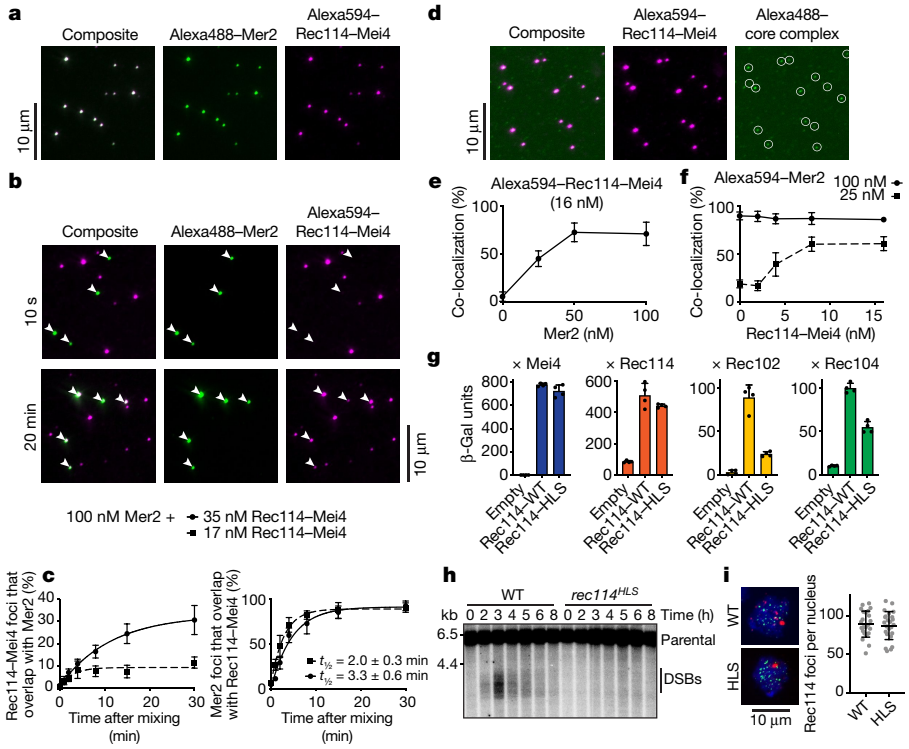

Fig. 4 | Tripartite Rec114–Mei4–Mer2 nucleoprotein condensates recruit the Spo11 core complex. a, Fluorescently labelled Rec114–Mei4 (17 nM) and Mer2 (100 nM) were mixed before DNA-driven condensation (for 30 min, 5.6 nM pUC19) and imaging by epifluorescence microscopy. **b**, Rec114–Mei4 and Mer2 nucleoprotein condensates were assembled separately for 10 min then mixed. After mixing, reactions contained 5.6 nM pUC19, 8.5 nM Alexa594–Rec114–Mei4 and 50 nM Alexa488–Mer2. Samples were dropped onto a microscope slide 10 s (top) or 20 min (bottom) after mixing. Arrowheads, Mer2 condensates. **c**, Time course of colocalization of Rec114–Mei4 and Mer2. The time to achieve 50% of Mer2 foci overlapping with Rec114–Mei4 is indicated ($t_{½}$). Lines are one-phase association models fit to the data. Data shown as mean ± s.d. from 9–10 fields of view. **d**, Incorporation of Alexa488-labelled core complexes[10] (circled, right) into Alexa594-labelled Rec114–Mei4–Mer2 condensates. **e**, Fraction of Rec114–Mei4 foci that contained detectable core complex signal as a function of Mer2 concentration. **f**, Fraction of Mer2 foci that contained detectable core complex signal as a function of Rec114–Mei4 concentration. Data shown as mean ± s.d. from 9–10 fields of view (**e**, **f**). **g**, Y2H interaction between Gal4AD–Rec114 (wild type or H39A/L40A/S41A (HLS) mutant) and LexA–Mei4, LexA–Rec114, LexA–Rec102, or LexA–Rec104 (mean + s.d. from four replicates). **h**, Southern blot analysis of meiotic DSB formation at the *CCT6* hotspot. **i**, Left, immunofluorescence microscopy of meiotic chromosome spreads with myc-tagged Rec114 (wild-type and HLS mutant strains). Green, anti-myc (Rec114); red, anti-Zip1; blue, DAPI. Right, number of Rec114 foci per leptotene or early zygotene cell ($n = 24$). Data shown as mean ± s.d. For gel source data, see Supplementary Fig. 1. See Source Data for exact n values (**c**, **f**).

weak interactions between recombinant proteins by affinity pull-down (Extended Data Fig. 7d). Moreover, XL–MS applied to mixtures of both complexes in the presence of DNA yielded numerous crosslinks between the Rec114 C-terminal domain and the coiled-coil region of Mer2, and between Mei4 and Mer2 at multiple positions along their lengths (Extended Data Fig. 7e).

RMM condensates recruit Spo11

When fluorescently labelled Spo11 core complexes bound to DNA were mixed with preassembled RMM–DNA condensates, the core complex signal overlapped with RMM foci (Fig. 4d). Recruitment of the core complex depended on Mer2 (Fig. 4e, Extended Data Fig. 8a). Rec114–Mei4 was also required when Mer2 was present at a low concentration (25 nM), but was dispensable at a high concentration of Mer2 (100 nM) (Fig. 4f, Extended Data Fig. 8b).

Rec114 interacts with Rec102 and Rec104 in Y2H assays[12,17]. Consistent with the idea that these interactions mediate the recruitment of core complexes to condensates, an excess of Rec102–Rec104 subcomplexes was able to outcompete the full core complex (Extended Data Fig. 8c, d).

We mapped the core complex-interacting domain of Rec114 by Y2H truncation analysis (Extended Data Fig. 8e). Deletion of about 50 amino acids from either the N or C termini of Rec114 abolished interaction with both Rec102 and Rec104, but deletion of the disordered region (residues 152–377) did not (Fig. 1a). By altering conserved residues in the N-terminal PH domain of Rec114, we identified a mutation (H39A/L40A/S41A, HLS) that specifically reduced interactions with Rec102 and Rec104 but did not affect the interaction with Mei4 or wild-type Rec114 (Fig. 4g), or the ability to make comingled RMM condensates in vitro (Extended Data Fig. 8f). The *rec114*^{HLS} mutant was defective for DSB formation (Fig. 4h) and gave inviable spores (Extended Data Fig. 8g), despite the mutant protein being expressed at normal levels (Extended Data Fig. 8h) and forming normal-looking chromatin-associated foci (Fig. 4i).

These data are consistent with the idea that the core complex is recruited to Rec114–Mei4–Mer2 condensates through at least two sets of interactions: one that depends on Mer2 and another involving contacts between the Rec114 PH domain and both Rec102 and Rec104.

Discussion

We have shown that Rec114–Mei4 and Mer2 form separate subcomplexes in vitro that each bind DNA with high cooperativity and assemble micrometre-scale nucleoprotein super-complexes that are reminiscent of biomolecular condensates that control a variety of processes[31–36]. These assemblies are reversible, can fuse both homotypically and heterotypically, and depend on multivalent protein–DNA and protein–protein interactions (Supplementary Discussion 3). Because mutations

that disrupt condensate formation also disrupt DSB formation in vivo, it appears that DNA-driven condensation is an important aspect of the initiation of recombination.

Meiotic chromosomes form chromatin loops that extend from a linear protein axis and it is thought that the DSB machinery assembled on axes captures and breaks loop DNA[5,16]. We propose that recruitment of Spo11 and regulatory components to RMM clusters forms the basis of this tethered loop–axis configuration (Extended Data Fig. 9a, Supplementary Discussion 4).

This model has notable implications. First, each cluster is likely to recruit multiple core complexes, which might explain how core complexes can be induced to dimerize[10] and how Spo11 can sometimes cut the same chromatid more than once[40,41]. RMM condensates may also provide platforms that display co-oriented arrays of Spo11 complexes, which could account for the observed 10-bp periodicity in the spacing between Spo11 cuts[41] (Extended Data Fig. 9a, Supplementary Discussion 4).

Second, RMM condensates may explain two previously unclear aspects of DSB patterning: hotspot competition, in which strong hotspots reduce the activity of neighbouring hotspots, and DSB interference, in which the DSB-responsive kinase Tel1 inhibits additional DSBs near an existing DSB[4] (Extended Data Fig. 9b, Supplementary Discussion 5). Hotspot competition could arise if nucleation of a condensate plus highly cooperative assembly locally depletes Rec114–Mei4 and Mer2 proteins, reducing the probability of another nucleation event. After a DSB is made, Tel1 may suppress additional DSBs nearby by acting both within and between adjacent condensates.

Third, the condensates may regulate DSB repair, for example by tethering and controlling the broken DNA ends and/or by nucleating formation of the recombination nodules at which repair takes place (Extended Data Fig. 9c, Supplementary Discussion 6).

In summary, our findings reveal how the DSB machinery self-organizes into punctate clusters that integrate DNA breakage with the loop–axis structure of chromosomes and that may thereby control DSB number, location and timing and coordinate DSB formation with downstream repair. DNA-driven RMM condensates therefore provide insight into how cells mitigate risks from the potentially dangerous generation of programmed DNA breaks during meiosis.

Online content

Any methods, additional references, Nature Research reporting summaries, source data, extended data, supplementary information, acknowledgements, peer review information; details of author contributions and competing interests; and statements of data and code availability are available at https://doi.org/10.1038/s41586-021-03374-w.

1. de Massy, B. Initiation of meiotic recombination: how and where? Conservation and specificities among eukaryotes. *Annu. Rev. Genet.* **47**, 563–599 (2013).
2. Lam, I. & Keeney, S. Mechanism and regulation of meiotic recombination initiation. *Cold Spring Harb. Perspect. Biol.* **7**, a016634 (2014).
3. Cooper, T. J., Garcia, V. & Neale, M. J. Meiotic DSB patterning: a multifaceted process. *Cell Cycle* **15**, 13–21 (2016).
4. Keeney, S., Lange, J. & Mohibullah, N. Self-organization of meiotic recombination initiation: general principles and molecular pathways. *Annu. Rev. Genet.* **48**, 187–214 (2014).
5. Kleckner, N. Chiasma formation: chromatin/axis interplay and the role(s) of the synaptonemal complex. *Chromosoma* **115**, 175–194 (2006).
6. Keeney, S., Giroux, C. N. & Kleckner, N. Meiosis-specific DNA double-strand breaks are catalyzed by Spo11, a member of a widely conserved protein family. *Cell* **88**, 375–384 (1997).
7. Bergerat, A. et al. An atypical topoisomerase II from Archaea with implications for meiotic recombination. *Nature* **386**, 414–417 (1997).
8. Robert, T. et al. The TopoVIB-Like protein family is required for meiotic DNA double-strand break formation. *Science* **351**, 943–949 (2016).
9. Vrielynck, N. et al. A DNA topoisomerase VI-like complex initiates meiotic recombination. *Science* **351**, 939–943 (2016).
10. Claeys Bouuaert, C. et al. Structural and functional characterization of the Spo11 core complex. *Nat. Struct. Mol. Biol.* **28**, 92–102 (2021).
11. Li, J., Hooker, G. W. & Roeder, G. S. *Saccharomyces cerevisiae* Mer2, Mei4 and Rec114 form a complex required for meiotic double-strand break formation. *Genetics* **173**, 1969–1981 (2006).
12. Maleki, S., Neale, M. J., Arora, C., Henderson, K. A. & Keeney, S. Interactions between Mei4, Rec114, and other proteins required for meiotic DNA double-strand break formation in *Saccharomyces cerevisiae*. *Chromosoma* **116**, 471–486 (2007).
13. Steiner, S., Kohli, J. & Ludin, K. Functional interactions among members of the meiotic initiation complex in fission yeast. *Curr. Genet.* **56**, 237–249 (2010).
14. Miyoshi, T. et al. A central coupler for recombination initiation linking chromosome architecture to S phase checkpoint. *Mol. Cell* **47**, 722–733 (2012).
15. Henderson, K. A., Kee, K., Maleki, S., Santini, P. A. & Keeney, S. Cyclin-dependent kinase directly regulates initiation of meiotic recombination. *Cell* **125**, 1321–1332 (2006).
16. Panizza, S. et al. Spo11-accessory proteins link double-strand break sites to the chromosome axis in early meiotic recombination. *Cell* **146**, 372–383 (2011).
17. Arora, C., Kee, K., Maleki, S. & Keeney, S. Antiviral protein Ski8 is a direct partner of Spo11 in meiotic DNA break formation, independent of its cytoplasmic role in RNA metabolism. *Mol. Cell* **13**, 549–559 (2004).
18. Sommermeyer, V., Béneut, C., Chaplais, E., Serrentino, M. E. & Borde, V. Spp1, a member of the Set1 complex, promotes meiotic DSB formation in promoters by tethering histone H3K4 methylation sites to chromosome axes. *Mol. Cell* **49**, 43–54 (2013).
19. Acquaviva, L. et al. The COMPASS subunit Spp1 links histone methylation to initiation of meiotic recombination. *Science* **339**, 215–218 (2013).
20. Kumar, R. et al. MEI4 — a central player in the regulation of meiotic DNA double-strand break formation in the mouse. *J. Cell Sci.* **128**, 1800–1811 (2015).
21. Stanzione, M. et al. Meiotic DNA break formation requires the unsynapsed chromosome axis-binding protein IHO1 (CCDC36) in mice. *Nat. Cell Biol.* **18**, 1208–1220 (2016).
22. Robert, T., Vrielynck, N., Mézard, C., de Massy, B. & Grelon, M. A new light on the meiotic DSB catalytic complex. *Semin. Cell Dev. Biol.* **54**, 165–176 (2016).
23. Tessé, S. et al. Asy2/Mer2: an evolutionarily conserved mediator of meiotic recombination, pairing, and global chromosome compaction. *Genes Dev.* **31**, 1880–1893 (2017).
24. Wang, W. et al. Homozygous mutations in REC114 cause female infertility characterised by multiple pronuclei formation and early embryonic arrest. *J. Med. Genet.* **57**, 187–194 (2020).
25. Kumar, R. et al. Mouse REC114 is essential for meiotic DNA double-strand break formation and forms a complex with MEI4. *Life Sci. Alliance* **1**, e201800259 (2018).
26. Kumar, R., Bourbon, H. M. & de Massy, B. Functional conservation of Mei4 for meiotic DNA double-strand break formation from yeasts to mice. *Genes Dev.* **24**, 1266–1280 (2010).
27. Boekhout, M. et al. REC114 partner ANKRD31 controls number, timing, and location of meiotic DNA breaks. *Mol. Cell* **74**, 1053–1068.e8 (2019).
28. Engebrecht, J. A., Voelkel-Meiman, K. & Roeder, G. S. Meiosis-specific RNA splicing in yeast. *Cell* **66**, 1257–1268 (1991).
29. Lorenz, A., Estreicher, A., Kohli, J. & Loidl, J. Meiotic recombination proteins localize to linear elements in *Schizosaccharomyces pombe*. *Chromosoma* **115**, 330–340 (2006).
30. Bonfils, S., Rozalén, A. E., Smith, G. R., Moreno, S. & Martín-Castellanos, C. Functional interactions of Rec24, the fission yeast ortholog of mouse Mei4, with the meiotic recombination-initiation complex. *J. Cell Sci.* **124**, 1328–1338 (2011).
31. Li, P. et al. Phase transitions in the assembly of multivalent signalling proteins. *Nature* **483**, 336–340 (2012).
32. Wheeler, J. R., Matheny, T., Jain, S., Abrisch, R. & Parker, R. Distinct stages in stress granule assembly and disassembly. *eLife* **5**, e18413 (2016).
33. Su, X. et al. Phase separation of signaling molecules promotes T cell receptor signal transduction. *Science* **352**, 595–599 (2016).
34. Boulay, G. et al. Cancer-specific retargeting of BAF complexes by a prion-like domain. *Cell* **171**, 163–178.e19 (2017).
35. Banani, S. F., Lee, H. O., Hyman, A. A. & Rosen, M. K. Biomolecular condensates: organizers of cellular biochemistry. *Nat. Rev. Mol. Cell Biol.* **18**, 285–298 (2017).
36. Boeynaems, S. et al. Protein phase separation: a new phase in cell biology. *Trends Cell Biol.* **28**, 420–435 (2018).
37. Lin, Y., Protter, D. S., Rosen, M. K. & Parker, R. Formation and maturation of phase-separated liquid droplets by RNA-binding proteins. *Mol. Cell* **60**, 208–219 (2015).
38. Patel, A. et al. A liquid-to-solid phase transition of the ALS protein FUS accelerated by disease mutation. *Cell* **162**, 1066–1077 (2015).
39. Xiang, S. et al. The LC domain of hnRNPA2 adopts similar conformations in hydrogel polymers, liquid-like droplets, and nuclei. *Cell* **163**, 829–839 (2015).
40. Garcia, V., Gray, S., Allison, R. M., Cooper, T. J. & Neale, M. J. Tel1(ATM)-mediated interference suppresses clustered meiotic double-strand-break formation. *Nature* **520**, 114–118 (2015).
41. Johnson, D. et al. Concerted cutting by Spo11 illuminates the mechanism of meiotic DNA break formation. *Nature* (in the press).
42. Dosztányi, Z. Prediction of protein disorder based on IUPred. *Protein Sci.* **27**, 331–340 (2018).

Methods

Preparation of expression vectors

Oligonucleotides (oligos) used in this study were purchased from Integrated DNA Technologies. The sequences of the oligos are listed in Supplementary Table 2. Plasmids are listed in Supplementary Table 3.

Separate exons of *S. cerevisiae REC114*, *MEI4* and *MER2* were amplified from genomic DNA of the SK1 strain and assembled by in-fusion cloning to yield intron-less pFastbac1-derived expression vectors pCCB649, pCCB652 and pCCB681, respectively. Primers for *REC114* were: cb906 and cb907 (exon 1), and cb908 and cb909 (exon 2). Primers for *MEI4* were: cb910 and cb911 (exon 1), and cb912 and 913 (exon 2). Primers for *MER2* were: cb978 and cb979 (exon 1), and cb980 and cb981 (exon 2). The genes were subcloned into pFastBac-HTb-Flag to generate N-terminally HisFlag-tagged expression vectors for HisFlag–Rec114 (pCCB650), Mei4 (pCCB653) and Mer2 (pCCB682). Maltose binding protein (*MBP*) was subcloned into the untagged vectors, to yield expression vectors for MBP–Rec114 (pCCB651) and MBP–Mei4 (pCCB654) and MBP–Mer2 (pCCB683).

To generate untagged Rec114–Mei4, the cleavage sequence for the TEV protease was introduced between the affinity tag and the sequence coding for Rec114 and Mei4 by inverse PCR and self-ligation using templates pCCB650 (primers cb1283 and cb1284) and pCCB654 (primers cb1287 and cb1288), to yield vectors pCCB789 (HisFlag–TEV–Rec114) and pCCB791 (MBP–TEV–Mei4), respectively. The mScarlet fluorophore was amplified from a synthetic gene codon-optimized for mammalian expression (gift from S. Kim, MSKCC) with primers cb1279 and cb1280 and cloned into the BamHI site of pCCB650 to yield pCCB786 (HisFlag–mScarlet–Rec114). A TEV cleavage site was further introduced between the affinity tag and the fluorophore by inverse PCR and self-ligation using template pCCB786 and primers cb1285 and cb1286 to yield pCCB790 (HisFlag–TEV–mScarlet–Rec114). The Rec114(R395A/K396A/K399A/K400A) (4KR) mutant was generated by inverse PCR and self-ligation of pCCB789 and pCCB790 with primers cb1332 and cb1334 to yield pCCB848 (HisFlag–TEV–Rec114(4KR)) and pCCB849 (HisFlag–TEV–mScarlet–Rec114(4KR)).

To generate a vector for Mer2 expression in *Escherichia coli*, *MER2* was amplified from pCCB681 using primers cb1161 and cb1162 and cloned into the BamHI site of pSMT3 to yield pCCB750 (SUMO–Mer2). eGFP-tagged Mer2 was generated by PCR amplification of eGFP using primers cb1259 and cb1260 and in-fusion cloning in the BamHI site of pCCB750 to yield pCCB777 (SUMO–eGFP–Mer2). The Mer2(K265A/R266A/R267A/R268A) (KRRR) mutation was generated by QuikChange mutagenesis using primers cb1186 and cb1187 of pCCB750 and pCCB777 to yield pCCB779 (SUMO–Mer2(KRRR)) and pCCB783 (SUMO–eGFP–Mer2(KRRR), respectively.

Full-length Rec114 and Mei4 were amplified from pCCB649 and pCCB650 using primers sp16 and sp17, and sp25 and sp26, respectively and cloned into the pETDuet-1 vector by in-fusion cloning to yield pSP34. A SUMO tag was introduced at the N terminus of Rec114 by PCR amplification of the pSMT3 vector with primers cb1172 and cb1180 and in-fusion cloning within the Nco1 and BamHI fragment of pSP34 to yield pSP53. Truncations were obtained from this construct by inverse PCR and self-ligation.

Expression vectors for purification of the core complex and Rec102–Rec104 from baculovirus-infected insect cells have previously been described[10].

Expression and purification of recombinant proteins

Viruses were produced using a Bac-to-Bac Baculovirus Expression System (Invitrogen) according to the manufacturer's instructions. We infected 2×10^9 *Spodoptera frugiperda* Sf9 cells (obtained from the J. Hurwitz laboratory, MSKCC) with combinations of viruses at a multiplicity of infection (MOI) of 2.5 each. Authentication of Sf9 cells and tests for mycoplasma contamination were conducted by the original supplier (Gibco, Thermo Fisher); no further tests for mycoplasma contamination were conducted. Expression of HisFlag–Rec114–MBP–Mei4 used viruses generated from pCCB650 and pCCB654, untagged Rec114–Mei4 used viruses generated from pCCB789 and pCCB791, and fluorescently tagged mScarlet–Rec114–Mei4 used viruses generated from pCCB790 and pCCB791. After 62 h infection, cells were collected, washed with phosphate buffer saline (PBS), frozen in dry ice and kept at −80 °C until use. All purification steps were carried out at 0–4 °C. Cell pellets were resuspended in 4 volumes of lysis buffer (25 mM HEPES-NaOH pH 7.5, 500 mM NaCl, 0.1 mM DTT, 20 mM imidazole, 1× Complete protease inhibitor tablet (Roche) and 0.1 mM phenylmethanesulfonyl fluoride (PMSF)). Cells were lysed by sonication and centrifuged at 43,000*g* for 30 min. The cleared extract was loaded onto 1 ml pre-equilibrated NiNTA resin (Qiagen). The column was washed extensively with nickel buffer (25 mM HEPES-NaOH pH 7.5, 500 mM NaCl, 10% glycerol, 0.1 mM DTT, 20 mM imidazole, 0.1 mM PMSF). The tagged complexes were then eluted in nickel buffer containing 250 mM imidazole. The complexes were further purified on amylose resin (NEB). Fractions containing protein were pooled and diluted in 3 volumes of amylose buffer (25 mM HEPES-NaOH pH 7.5, 500 mM NaCl, 10% glycerol, 2 mM DTT, 5 mM EDTA). Next, the complexes were bound to 1 ml of the amylose resin in a poly-prep chromatography column (Bio-Rad) and the resin was washed extensively. Complexes were eluted from amylose resin with buffer containing 10 mM maltose. Fractions containing protein were pooled and loaded on a Superdex 200 column preequilibrated with Amylose buffer. For untagged or mScarlet-tagged complexes, samples were treated with an excess of TEV protease before gel filtration. For fluorescently labelled complexes, labelling was performed using Alexa Fluor 594 (Invitrogen no. A10239), which has a succinimidyl ester moiety that reacts with primary amines. After 1 h conjugation at room temperature, complexes were purified by gel filtration. Fractions containing protein were concentrated in 50 kDa cutoff Amicon centrifugal filters (Millipore). Aliquots were frozen in dry ice and stored at −80 °C.

For expression of recombinant proteins in *E. coli*, expression vectors were transformed in BL21 DE3 cells and plated on LB plates containing the appropriate antibiotic. Cells were then cultured in liquid medium at 37 °C to an optical density (OD_{600}) of 0.6. For Mer2 proteins and variants, expression was carried out at 30 °C for 3 h with 1 mM isopropyl β-D-1-thiogalactopyranoside (IPTG). For Rec114–Mei4 truncations, expression was carried out at 16 °C overnight with 0.2 mM IPTG. Cells were resuspended in nickel buffer (25 mM HEPES-NaOH pH 7.5, 500 mM NaCl, 10% glycerol, 0.1 mM DTT, 20 mM imidazole, 0.1 mM PMSF) and frozen dropwise in liquid nitrogen and kept at −80 °C until use. All the purification steps were carried out at 0–4 °C. Cells were lysed using a French press and centrifuged at 43,000*g* for 30 min. The cleared extract was loaded onto 1 ml pre-equilibrated NiNTA resin (Qiagen). The column was washed extensively with nickel buffer then eluted in buffer containing 250 mM imidazole. The 6His–SUMO tag was cleaved with Ulp1 during overnight dialysis in gel filtration buffer (25 mM HEPES-NaOH pH 7.5, 300 mM NaCl, 10% glycerol, 40 mM imidazole, 1 mM DTT, 5 mM EDTA). The sample was then loaded on a second nickel column to remove 6His–SUMO and Ulp1. The flow-through was then loaded on a Superdex 200 column preequilibrated with gel filtration buffer. For Mer2 complexes labelled with Alexa Fluor 488 (Invitrogen no. A10235), fluorophore conjugation was performed at room temperature for 1 h before gel filtration. Alexa Fluor 488 has a tetrafluorophenyl ester moiety that reacts with primary amines. After gel filtration, fractions containing protein were concentrated in 10-kDa cutoff Amicon centrifugal filters (Millipore). Aliquots were frozen in dry ice and stored at −80 °C.

Purification of Alexa^{488}-labelled Spo11 core complexes was achieved essentially as previously described[10], except with an additional fluorophore conjugation step before gel filtration. In brief, Spo11–HisFlag, Ski8, Rec102 and Rec104 were expressed in *S. frugiperda* Sf9 cells by co-infection with a combination of baculoviruses coding for individual subunits. Cells were collected 62 h after infection and the complexes

purified by sequential affinity chromatography on NiNTA resin and anti-Flag resin. Complexes were dialysed in buffer containing 25 mM HEPES-NaOH pH 7.5, 500 mM NaCl, 10% glycerol, 2 mM DTT and 5 mM EDTA, then conjugated to Alexa Fluor 488 (Invitrogen no. A10235) by 1-h incubation at room temperature and purified by size exclusion chromatography on a Superdex 200 column. Finally, fractions containing protein were concentrated and aliquots stored at −80 °C. Rec102–Rec104 complexes were purified by co-infection of Sf9 cells with viruses expressing MBP–Rec102 and Rec104–HisFlag. Complexes were purified by sequential affinity chromatography on NiNTA resin and amylose resin, using the same procedure as for the core complex[10].

SEC–MALS

Light scattering data in Fig. 1c, h were collected using a Superdex 200, 10/300, HR Size Exclusion Chromatography (SEC) column (GE Healthcare), connected to a High Performance Liquid Chromatography System (HPLC), Agilent 1200, (Agilent Technologies) equipped with an autosampler. The elution from SEC was monitored by a photodiode array (PDA) UV/VIS detector (Agilent Technologies), differential refractometer (OPTI-Lab rEx Wyatt), and a static and dynamic, multiangle laser light scattering (LS) detector (HELEOS II with QELS capability, Wyatt). The SEC–UV/LS/RI system was equilibrated in buffer 25 mM Hepes pH 7.5, 500 mM NaCl, 10% glycerol, 2 mM EDTA at a flow rate of 0.5 ml/min or 1.0 ml/min. Two software packages were used for data collection and analysis: Chemstation software (version B.04.03-SP1, Agilent Technologies) controlled the HPLC operation and data collection from the multi-wavelength UV/VIS detector, and ASTRA V software (Wyatt) collected data from the refractive index detector and the light scattering detectors, and recorded the UV trace at 280 nm sent from the PDA detector. The weight average molecular masses were determined across the entire elution profile at intervals of 1 s from static LS measurement using ASTRA software.

All other SEC–MALS experiments were performed with an Äkta-MALS system. Proteins (500 µl) were loaded on Superdex 75 10/300 GL or Superdex 200 10/300 GL columns (GE Healthcare) and eluted with buffer 20 mM Tris pH 7.5, 300 mM NaCl, 2 mM DTT at a flow rate of 0.3 ml/min. The light scattering was monitored by a miniDAWN TREOS system (Wyatt Technologies) and concentration was measured with an Optilab T-rEX differential refractometer (Wyatt Technologies).

Crosslinking and mass spectrometry

For crosslinking of purified proteins, about 20–50 µg of HisFlag–Rec114–MBP–Mei4 or HisFlag–Mer2 complexes were incubated in 50–100-µl reactions in the presence of 2 mM disuccinimidyl suberate (DSS) in buffer containing 25 mM HEPES-NaOH pH 7.5, 500 mM NaCl, 10% glycerol, 2 mM DTT and 5 mM EDTA. For crosslinking of condensates, 900 µl reactions containing 30 µg of HisFlag–Rec114–MBP–Mei4 and 20 µg of Mer2 complexes in 20 mM HEPES-NaOH pH 7.5, 100 mM NaCl, 5% glycerol, 5 mM $MgCl_2$ and 100 ng/µl pUC19 were incubated at 30 °C before the addition of 2 mM DSS. After 10 min crosslinking at 30 °C, reactions were quenched with 100 mM Tris-HCl pH 7.5. Crosslinked proteins were separated by SDS–PAGE and stained with SimplyBlue (Invitrogen). Protein bands were excised and digested in situ with trypsin as previously described[43]. The tryptic peptides were purified using a 2-µl bed volume of Poros 50 R2 (Applied Biosystems) reverse-phase beads packed in Eppendorf gel-loading tips[44]. The digested peptides were diluted in 0.1% formic acid, and each sample was analysed separately by microcapillary LC with tandem MS using the NanoAcquity system (Waters) with a 100 µm inner diameter × 10 cm length C18 column (1.7 µm BEH130; Waters) configured with a 180 µm × 2 cm trap column coupled to a Q-Exactive Plus mass spectrometer (Thermo Fisher Scientific). A proxeon nanoelectrospray source set at 1,800 V and a 75-µm (with 10-µm orifice) fused silica nano-electrospray needle (New Objective) were used to complete the interface. One microlitre of sample was loaded onto the trap column and washed with 3× loop volume of buffer A (0.1% formic acid), and the flow was reversed through the trap column and the peptides eluted with a 1–50% acetonitrile (with 0.1% formic acid) gradient over 50 min at a flow rate of 300 nl/min over the analytical column. The QE Plus was operated in automatic, data-dependent MS/MS acquisition mode with one MS full scan (370–1,700 m/z) at 70,000 mass resolution and up to ten concurrent MS/MS scans for the ten most intense peaks selected from each survey scan. Survey scans were acquired in profile mode and MS/MS scans were acquired in centroid mode at 17,500 resolution and isolation window of 1.5 amu. AGC was set to 1×10^6 for MS1 and 5×10^5 and 100 ms maximum IT for MS2. Charge exclusion of 1, 2 and greater than 8 was enabled with dynamic exclusion of 15 s. To analyse the cross-linked peptides we used pLink[45]. The raw MS data were analysed using pLink search with the following parameters: precursor mass tolerance 50 ppm, fragment mass tolerance 10 ppm, cross-linker DSS (cross-linking sites K and protein N terminus), xlink mass-shift 138.068, monolink mass-shift 156.079, fixed modification C 57.02146, variable modification oxidized methionine, deamidation N,Q, protein N-acetyl, peptide length minimum 4 amino acids and maximum 100 amino acids per chain, peptide mass minimum 400 and maximum 10,000 Da per chain, enzyme trypsin, two missed cleavage sites per chain (four per cross-link). The data were imported on the xiNET online tool to generate crosslinking maps[46]. All identified crosslinks can be found in Supplementary Table 1.

To estimate the ratio of Rec114 and Mei4 by mass spectrometry, 10 µg of HisFlag–Rec114–MBP–Mei4 was digested with trypsin and analysed by tandem MS as described above, and spectral counts of the two proteins were compared, omitting the tags. Rec114 and Mei4 have similar lengths (428 and 408 amino acids, respectively), and similar numbers of K and R residues (56 and 66, respectively). The average and median trypic peptide lengths are 7.6 and 5 for Rec114 and 6.1 and 4 for Mei4, respectively. The .raw files were converted to .mgf and searched by Mascot (Matrix Science, version 2.6.100) using the Fasta formatted Swissprot reviewed database (downloaded 5 July 2017 from https://www.uniprot.org/) and the Fasta formatted Rec114 and Mei4 sequence. The search parameters were as follows: (i) two missed cleavage tryptic sites were allowed; (ii) precursor ion mass tolerance 10 ppm; (iii) fragment ion mass tolerance 0.08 Da (monoisotopic); (iv) fixed modification of carbamidomethyl of cysteine; and (v) variable protein modifications were allowed for methionine oxidation, deamidation on NQ, protein N-terminal acetylation, and phospho STY. Scaffold (version Scaffold_4.8.4, Proteome Software) was used to validate MS/MS-based peptide and protein identifications. Peptide identifications were accepted if they could be established at greater than 70% probability to achieve a false discovery rate (FDR) of less than 1% by the Scaffold Local FDR algorithm. Protein identifications were accepted if they could be established at greater than 6% probability to achieve an FDR less than 1% and contained at least two identified peptides. Protein probabilities were assigned by the Protein Prophet algorithm[47]. Proteins that contained similar peptides and could not be differentiated based on MS/MS analysis alone were grouped to satisfy the principles of parsimony. Proteins sharing significant peptide evidence were grouped into clusters.

AFM imaging

For AFM imaging of Rec114–Mei4 or Mer2 bound to plasmid DNA, protein complexes were diluted to the indicated concentration (12–50 nM) in the presence of 1 nM supercoiled pUC19 in 25 mM HEPES-NaOH pH 6.8, 5 mM $MgCl_2$, 50 mM NaCl, 10% glycerol. Complexes were assembled at 30 °C for 30 min. A volume of 40 µl of the protein–DNA binding reaction was deposited onto freshly cleaved mica (SP1) for 2 min. The sample was rinsed with 10 ml ultrapure deionized water and the surface was dried using a stream of nitrogen. AFM images were captured using an Asylum Research MFP-3D-BIO (Oxford Instruments) microscope in tapping mode at room temperature. An Olympus AC240TS-R3

AFM probe with resonance frequencies of approximately 70 kHz and spring constant of approximately 1.7 N/m was used for imaging. Images were collected at a speed of 0.5–1 Hz with an image size of 2 µm at 2,048 × 2,048-pixel resolution.

DNA substrates and gel shift assays

Short linear DNA substrates were generated by annealing complementary oligos (sequences listed in Supplementary Table 2). The substrates were the following (with oligo names in parentheses): dsDNA20 (cb939 and cb940), dsDNA40 (cb922 and cb935), dsDNA80 (cb95 and cb100). The 80-nt oligos were first purified on 10% polyacrylamide-urea gels. Oligos were subsequently mixed in equimolar concentrations (10 µM) in STE (100 mM NaCl, 10 mM Tris-HCl pH 8, 1 mM EDTA), heated and slowly cooled on a PCR thermocycler (98 °C for 3 min, 75 °C for 1 h, 65 °C for 1 h, 37 °C for 30 min, 25 °C for 10 min). For radioactive labelling, 1/20th of the annealed substrates were 5′-end-labelled with [γ-^{32}P]-ATP (Perkin Elmer) and T4 polynucleotide kinase (New England Biolabs). Labelled and unlabelled substrates were purified by native polyacrylamide gel electrophoresis. Larger linear substrates were prepared by PCR amplification of a 9.6-kb template derived from pUC19 (pDR470). Substrates were as follows: 100 bp (cb343 and cb1339), 1,000 bp (cb342 and cb343), 9.6 kb (cb1175 and cb1177 or cb343 and cb1338). Fluorescently labelled substrates were prepared by PCR amplification of pDR470 as follows: Cy3–100 bp (cb1330 and cb1339), Cy3–9.6 kb (cb1330 and cb1338), Cy5–100 bp (cb1331 and cb1339), Cy5–9.6 kb (cb1331 and cb1338). PCR products were purified by agarose gel electrophoresis.

Short double-stranded DNA substrates were prepared by annealing the following complementary oligos: 20 bp (cb939 and cb940), 40 bp (cb922 and cb935), 80 bp (cb95 and cb100). Substrates were labelled with [γ-^{32}P]-ATP by polynucleotide kinase and gel purified. Binding reactions (20 µl) were carried out in 25 mM Tris-HCl pH 7.5, 7.5% glycerol, 100 mM NaCl, 2 mM DTT and 1 mg/ml BSA with 1 mM EDTA or 5 mM $MgCl_2$, when indicated. Unless stated otherwise, reactions contained 2 nM pUC19 or 0.5 nM radiolabelled substrate and the indicated concentration of protein. Concentrations for Rec114–Mei4 were calculated on the basis of a 2:1 stoichiometry. For Mer2, the concentrations are expressed as monomers. Complexes were assembled for 30 min at 30 °C and separated by gel electrophoresis. For plasmid substrates, binding reactions were loaded on a 0.5% agarose (Gold) gel in 40 mM Tris-acetate buffer supplemented with 1 mM EDTA or 5 mM $MgCl_2$, as indicated, at 50 V for 2.5 h. Gels were stained with ethidium bromide and scanned using a ChemiDoc Imaging System (Bio-Rad). For short substrates, binding reactions were separated on 8% TAE-polyacrylamide gels at 200 V for 2 h, and gels were dried and imaged by autoradiography.

In vitro condensation assays

DNA-driven condensation reactions were assembled as follows: RMM proteins were first diluted to 5 µl in storage buffer adjusted to a final salt concentration of 360 mM NaCl. After 5 min at room temperature, condensation was induced by threefold dilution in reaction buffer containing DNA and no salt, to reach final 15-µl reactions that contained 25 mM Tris-HCl pH 7.5, 5% glycerol, 120 mM NaCl, 2 mM DTT, 1 mg/ml BSA, 5 mM $MgCl_2$, 5% PEG 8000, unless indicated otherwise. A typical binding reaction contained 150 ng supercoiled pUC19 (5.7 nM), 50–200 nM Mer2 (Alexa488–Mer2 or eGFP–Mer2) and/or 8–35 nM Rec114–Mei4 (Alexa594–Rec114–Mei4 or mScarlet–Rec114–Mei4). For experiments with core complexes, binding reactions containing 25 nM Alexa488–core complex with or without 200 nM MBP–Rec102–Rec104–HisFlag competitor were assembled for 10 min, then mixed with an equal volume of reactions containing Rec114–Mei4–Mer2 condensates. After 30 min incubation at 30 °C with occasional mixing, 4 µl was dropped on a microscope slide and covered with a coverslip. Images were captured on a Zeiss Axio Observer Z1 Marianas Workstation with a 100×/1.4 NA oil immersion objective. Marianas Slidebook (Intelligent Imaging Innovations) software was used for acquisition. Images were analysed with ImageJ using a custom-made script. In brief, 129.24 × 129.24-µm (2,048 × 2,048-pixel) images were thresholded using the mean intensity of the background plus three times the standard deviation of the background. For experiments in which the number of foci was compared between wild-type and mutant proteins or between reactions with and without Mg^{2+}, a fixed threshold was applied. Masked foci were counted and the intensity inside the foci mask was integrated. Data points represent averages of at least 8–10 images per sample. Data were analysed using Graphpad Prism 8.

Yeast strains and targeting vectors

Yeast strains were from the SK1 background. All strains used in this study are listed in Supplementary Table 4 and were validated by genotyping by PCR and/or Southern blot analysis. When constructed by crosses, genotypes were validated by segregation of linked genetic markers.

Strains that have endogenous *MER2* replaced by *kanMX4* cassette (SKY1524 and SKY1525) have previously been described[15]. *MER2myc5::URA3* was inserted at the *mer2Δ::kanMX4* locus by EcoRI linearization of pRS306-derived pSK351 (WT) and pJX005 (KRRR) and transformation into SKY1524 and SKY1525 to yield SKY1560 and SKY1695 (WT), and SKY6411 and SKY6413 (KRRR). Integration of the vectors was confirmed by PCR.

Strains that have endogenous *REC114* replaced by the *kanMX4* cassette (SKY865 and SKY866) have previously been described[12]. Tagged and untagged *REC114* alleles were generated by transformation of SKY865 and SKY866 with AflII-digested plasmids pRS305-derived targeting vectors. Plasmids and resultant strains were as follows: *REC114–8myc* (pSK591, SKY6749 and SKY6750), *REC114* (pSK592, SKY6562 and SKY6563), *rec114(F411A)–8myc* (pCCB857, SKY6889 and SKY6890), r*ec114(F411A)* (pCCB856, SKY6885 and SKY6886), *rec114(4KR)–8myc* (pCCB851, SKY6859 and SKY6860), *rec114(HLS)–8myc* (pSP113, SKY6797 and SKY6798).

Y2H vectors for wild-type DSB proteins were as previously described[12,17]. pACT2-derived plasmids carry the *LEU2* marker and express the Gal4-activator domain. pCA1-derived plasmids carry the *TRP1* marker and express the DNA-binding domain of LexA. The vectors used here were as follows: pACT2-Rec114 (pSK304) encodes Gal4AD–Rec114, pCA1-Mei4 (pSK281) encodes LexA–Mei4, pCA1-Rec102 (pSK282) encodes LexA–Rec102, pCA1-Rec104 (pSK283) encodes LexA–Rec104. Gal4AD empty vector control (pACT2) was pSK276. Y2H vectors for Rec114 truncations were generated by inverse PCR and self-ligation of the full-length construct pSK304. Plasmid numbers were as follows: Rec114(152–277) (pSP9), Rec114(del1–50 and 152–277) (pSP1), Rec114(del101–277) (pSP3), Rec114(del152–377) (pSP6). Rec114(53–428) and Rec114(1–377) were as previously reported[12]. Point mutants were made by QuikChange mutagenesis and were as follows: Rec114(HLS) (pSP25), Rec114(F411A) (pCCB858).

Immunofluorescence of yeast nuclei spreads

Diploid strains were cultured overnight in YPD (1% yeast extract, 2% peptone, 2% dextrose), followed by 13.5–14 h in YPA (1% yeast extract, 2% peptone, 2% potassium acetate (KOAc)). Meiosis was induced by transfer to 2% KOAc. After 3.5 h, cells were collected, washed with H_2O, resuspended in 1 M sorbitol, 1× PBS pH 7, 10 mM DTT, and 0.5 mg/ml zymolyase 20T, and incubated for 30 min at 30 °C with gentle shaking. Spheroplasts were collected by centrifugation at 1,500*g*, washed in ice-cold 100 mM MES, 1 M sorbitol, spun down, then lysed in ice-cold 20 mM MES, 3% paraformaldehyde and spread on a microscope slide for 1 h. Slides were washed three times with 1 ml 0.4% PhotoFlo 200 solution (Kodak), air dried and stored at −20 °C. Slides were blocked with 90% FBS, 1 × PBS for 1 h at room temperature in a humid chamber, then incubated with primary antibody diluted in 3% BSA, 1 × PBS in a humid chamber at 4 °C. After 3 × 5-min washes with 1 × PBS in a Coplin jar, slides were incubated with secondary antibody diluted in 3% BSA, 1 × PBS in a

humid chamber at 37 °C for 1 h. Slides were washed in the dark for 3 × 5 min with 1 × PBS, and mounted with Vectashield containing DAPI (Vector Labs). Primary antibodies used were mouse monoclonal anti-myc antibody clone 9E10 (1/100, Abcam) and rabbit polyclonal anti-Zip1 (1/50, this laboratory). Secondary antibodies used were goat anti-mouse IgG Alexa-488 and donkey anti-rabbit IgG Alexa-594 (1/200, Molecular Probes). Images of nuclei spreads were acquired on a Zeiss Axio Observer Z1 Marianas Workstation, equipped with an ORCA-Flash 4.0 camera and DAPI, FITC and Texas red filter sets, illuminated by an X-Cite 120 PC-Q light source, with a 100×/1.4 NA oil immersion objective. Marianas Slidebook software (Intelligent Imaging Innovations) was used for acquisition. Images were analysed in Image J. Staging of nuclei spreads was based on DAPI staining and Zip1 immunufluorescence patterns, with nuclei showing a diffuse DAPI signal with either a single bright Zip1 focus or a few small Zip1 foci counted as leptotene or zygotene cells, respectively.

Southern blot analysis of DSBs

Meiotic DSB analysis by Southern blotting was performed as previously described[48]. In brief, synchronized cultures undergoing meiosis were collected at the indicated time. After DNA purification, 800 ng of genomic DNA was digested by PstI and separated on a 1% TBE-agarose gel. DNA was transferred to Hybond-XL nylon membranes by vacuum transfer, hybridized with *SLY1* probe (amplified with primers: 5′-GCGTCCCGCAAGGACATTAG, 5′-TTGTGGCTAATGGTTTTGCGGTG) and developed by autoradiography.

Spo11-oligo labelling

The procedure for labelling Spo11-associated oligos has previously been described[49]. In brief, yeast cultures were collected 4 h into meiosis and denatured extracts were prepared by trichloroacetic acid precipitation. Proteins were solubilized in 2% SDS, 500 mM Tris-HCl pH 8.1, 10 mM EDTA. Extracts were diluted in an equal volume of 2 × IP Buffer (2% Triton X100, 30 mM Tris-HCl pH 8.1, 300 mM NaCl, 2 mM EDTA, 0.02% SDS) and Flag-tagged Spo11–oligo complexes were immunoprecipitated on IgG-conjugated agarose beads with mouse monoclonal M2 anti-Flag antibody. DNA was labelled on the beads with terminal deoxynucleotidyl transferase and [α-^{32}P]dCTP. After washing the beads in 1 × IP buffer, proteins were eluted with LDS sample buffer and separated by SDS–PAGE. The gel was dried and developed by autoradiography.

Western blotting of yeast meiotic extracts

Denaturing whole-cell extracts were prepared in 10% trichloroacetic acid with agitation in the presence of glass beads. Precipitated proteins were solubilized in Laemmli sample buffer and appropriate amounts of protein were separated by SDS–PAGE and analysed by western blotting. Antibodies were mouse monoclonal anti-myc (1/2,000, Abcam), rabbit polyclonal anti-Kar2 (y-115) (1/2,000, Santa Cruz), HRP-conjugated mouse monoclonal anti-Flag M2 (1:2,000, Sigma), mouse monoclonal anti-MBP (1:2,000, NEB). Secondary antibodies were used at 1/5,000: IRDye 800CW goat anti-mouse IgG and IRDye 680 goat anti-rabbit IgG. Western blots were revealed using the Li-COR Bioscience Odyssey infrared imaging system.

Yeast two hybrid

Y2H vectors were transformed separately in haploid strains SKY661 and SKY662 and selected on appropriate synthetic dropout medium. Strains were mated and streaked for single diploid colonies on medium lacking tryptophan and leucine. Single colonies were grown overnight in selective medium containing 2% glucose. Cultures were diluted in fresh medium containing 2% galactose and 1% raffinose and grown until log phase (4 h). Cells were lysed and a quantitative β-galactosidase assay was performed using ONPG substrate according to standard protocols (Clontech Laboratories).

Fluorescence recovery after photobleaching

Fluorescence recovery after photobleaching (FRAP) experiments were performed on a ZEISS LSM 880 confocal microscope at room temperature. Condensates were assembled in 15-µl reactions with 200 nM Alexa488–Mer2 or 20 nM Alexa594–Rec114–Mei4 mixed with 150 ng pUC19 plasmid DNA in buffer containing 25 mM Tris-HCl pH 7.5, 5% glycerol, 120 mM NaCl, 2 mM DTT, 1 mg/ml BSA, 5 mM $MgCl_2$, and 5% PEG 8000, incubated at 30 °C for 30 min, then loaded into a 384-well glass-bottom microplate (Greiner bio-one) pre-coated with 1 mg/ml BSA (Sigma). Droplets were photobleached with 20% laser power for 1 s using 488-nm and 594-nm lasers. Time-lapse images were acquired with a 10-s interval and processed using FIJI. Fluorescence intensities of regions of interest were corrected by unbleached control regions and then normalized to pre-bleached intensities.

Pulldown assay

HisFlag–Rec114–MBP–Mei4 complexes were expressed in 50-ml Sf9 cultures and purified by sequential affinity chromatography on NiNTA resin and amylose resin following a similar procedure as described above. After immobilization on amylose, one-sixth (50 µl) of the resin was equilibrated in buffer containing 25 mM Hepes pH 7.5, 150 mM NaCl, 10% glycerol, 1 mM DTT, 2 mM EDTA, and 0.1% Triton. Resin without Rec114–Mei4 complexes was used as a control. The resin was incubated with 500 µl of buffer containing 5 µg of purified Mer2. After 30 min of incubation on a rotating wheel at 4 °C, the resin was collected by gentle centrifugation, washed twice with 1 ml buffer, the proteins were resuspended in Laemmli buffer and analysed by SDS–PAGE.

Partial proteolysis

For Mer2 (wild-type or KRRR mutant), 2 µg protein was digested in 20-µl reactions in 100 mM Tris-HCl pH 8, 12.5 mM HEPES-NaOH pH 7.5, 150 mM NaCl, 5% glycerol, 2.5 mM EDTA, 0.5 mM DTT and the indicated amount of trypsin. For HisFlag–Rec114–MBP–Mei4 (wild-type or 4KR), 1 µg protein was digested in 30-µl reactions containing 100 mM Tris-HCl pH 8, 20 mM HEPES-NaOH pH 7.5, 240 mM NaCl, 8% glycerol, 4 mM EDTA, 0.8 mM DTT and the indicated amount of trypsin. After 30 min at room temperature, reactions were stopped with 0.2 mM PMSF and Laemmli buffer, and proteins were analysed by SDS–PAGE.

Statistics and reproducibility

Micrographs shown in the article are representative images to illustrate the observations. Sample numbers in quantifications are indicated in the figure legends. Fig. 1b, g: purified proteins were analysed by gel electrophoresis more than three times. Fig. 2c: condensates were imaged by AFM at least three times, typically with dozens of condensates observed for each experiment. Protein complexes without DNA were imaged at least twice in different buffers with similar results. Fig. 2d: quantification is shown for a time course performed once, but the pattern was confirmed at least once independently. Fig. 3a: quantification is shown for one experiment, but the DNA-binding defect of the mutant was confirmed at least twice independently using different substrates. Fig. 3b: quantification is shown for one experiment, but the condensation defect of the mutant was confirmed at least twice independently in different conditions. Fig. 3c: quantification is shown with data pooled from two cultures. The observation was reproduced at least twice independently. Fig. 3d: Southern blot analysis was performed with two independent cultures with identical results. Fig. 4a: co-localization was observed more than three times in different conditions. Fig. 4b: the pattern was observed at least twice independently. Fig. 4c: quantification is shown for a time course performed once. Fig. 4d: the observation was reproduced more than three times. Fig. 4e: quantification is shown for a titration performed once. Fig. 4g: quantification is shown for an experiment with four replicates. The experiment

was repeated once with similar results. Fig. 4h: Southern blot is shown for a time course performed once. Fig. 4i: quantification is shown with data pooled from two independent cultures. Extended Data Fig. 1b, g, i: observations were reproduced at least once independently. Extended Data Fig. 1l: Southern blot is shown for a time course performed once. Extended Data Fig. 1g: quantification is shown for an experiment with four replicates. The experiment was repeated once with similar results. Extended Data Fig. 1n: the experiment was performed with two independent cultures with identical results. Extended Data Fig. 2a, b: titrations were repeated at least once with identical results. Extended Data Fig. 2c, d: competition was performed once. Extended Data Fig. 2e, f: the observations were reproduced at least twice independently. Extended Data Fig. 2g: condensates were imaged by AFM at least three times, typically with dozens of condensates observed for each experiment. Protein complexes without DNA were imaged at least twice in different buffers with similar results. Extended Data Fig. 4g, h: observation reproduced at least once independently. Extended Data Fig. 6a, c: truncation analyses were performed at least twice. Extended Data Fig. 6b, d: quantifications are shown for one experiment, but the DNA-binding and condensation defects of the mutant was confirmed at least twice independently in different conditions. Extended Data Fig. 6g: experiments were performed with two independent cultures with identical results. Extended Data Fig. 6h: patterns were confirmed at least once. Extended Data Fig. 6i: time course was performed once. Extended Data Fig. 6j: Southern blot analysis was performed with two independent cultures with identical results. Extended Data Fig. 7a: experiment was performed once. Extended Data Fig. 7c: experiment was performed at least twice. Extended Data Fig. 7d: pulldown was repeated at least twice independently. No statistical methods were used to predetermine sample size. Investigators were not blinded to allocation during experiments and outcome assessment.

Reporting summary

Further information on research design is available in the Nature Research Reporting Summary linked to this paper.

Data availability

Processed crosslinking-mass spectrometry data are provided in Supplementary Table 1. Fasta sequences of the yeast SK1 strain are available at https://www.yeastgenome.org. Swissprot reviewed database is available at https://www.uniprot.org/. Source data are provided with this paper.

Code availability

The custom ImageJ scripts for analysis of condensate foci are available at https://github.com/claeysbouuaert/scripts.

43. Sebastiaan Winkler, G. et al. Isolation and mass spectrometry of transcription factor complexes. *Methods* **26**, 260–269 (2002).
44. Erdjument-Bromage, H. et al. Examination of micro-tip reversed-phase liquid chromatographic extraction of peptide pools for mass spectrometric analysis. *J. Chromatogr. A* **826**, 167–181 (1998).
45. Yang, B. et al. Identification of cross-linked peptides from complex samples. *Nat. Methods* **9**, 904–906 (2012).
46. Combe, C. W., Fischer, L. & Rappsilber, J. xiNET: cross-link network maps with residue resolution. *Mol. Cell. Proteomics* **14**, 1137–1147 (2015).
47. Nesvizhskii, A. I., Keller, A., Kolker, E. & Aebersold, R. A statistical model for identifying proteins by tandem mass spectrometry. *Anal. Chem*. **75**, 4646–4658 (2003).
48. Murakami, H., Borde, V., Nicolas, A. & Keeney, S. Gel electrophoresis assays for analyzing DNA double-strand breaks in *Saccharomyces cerevisiae* at various spatial resolutions. *Methods Mol. Biol*. **557**, 117–142 (2009).
49. Neale, M. J. & Keeney, S. End-labeling and analysis of Spo11-oligonucleotide complexes in *Saccharomyces cerevisiae*. *Methods Mol. Biol*. **557**, 183–195 (2009).

Acknowledgements We thank A. Nicolas and V. Borde for sharing unpublished information; J. Xu for assistance with preliminary analyses of the Mer2(KRRR) mutant; other members of the Keeney lab for discussions; MSK core facilities, supported by NIH cancer center core grant P30 CA008748: Microchemistry and Proteomics (R. Hendrickson and E. Chang) for the XL–MS experiments; Molecular Cytology (M. Brendel and Y. Romin) for AFM experiments; S. Fujisawa for writing a Fiji script to quantify fluorescent foci; and E. Folta-Stogniew from the Biophysics Resource of Keck Facility at Yale University for the SEC-MALS experiments. The SEC–LS/UV/RI instrumentation was supported by NIH grant S10 RR023748. This work was supported by the Howard Hughes Medical Institute (S.K.), the Maloris Foundation (D.P.), an MSK Basic Research Innovation Award (S.K. and D.P.), the European Research Council under the European Union's Horizon 2020 research and innovation program (ERC grant agreement 802525 to C.C.B.), and the Fonds National de la Recherche Scientifique (MIS-Ulysse grant F.6002.20 to C.C.B.).

Author contributions C.C.B. and S.K. designed the study and supervised the research; C.C.B. carried out all experiments except as noted; S.P. performed yeast two-hybrid experiments (Fig. 4g, Extended Data Figs. 1k, 8e) and assisted C.C.B. with the generation of expression constructs, virus preparation and protein purification; J.W. performed SEC–MALS analyses of mutant protein constructs (Fig. 1j, Extended Data Fig. 1h, j) and W.X. performed FRAP experiments (Extended Data Fig. 5c) under the supervision of D.J.P.; C.O. performed MBP pulldown (Extended Data Fig. 7d) and trypsin proteolysis experiments (Extended Data Fig. 6h) and D.D. performed the condensate mixing experiments (Extended Data Figs. 6e, 8f) under the supervision of C.C.B.; C.C.B. and S.K. wrote the paper with input from the other authors; C.C.B., D.J.P. and S.K. secured funding.

Competing interests The authors declare no competing interests.

Additional information
Supplementary information The online version contains supplementary material available at https://doi.org/10.1038/s41586-021-03374-w.

Correspondence and requests for materials should be addressed to C.C.B. or S.K.

Peer review information *Nature* thanks the anonymous reviewers for their contribution to the peer review of this work.

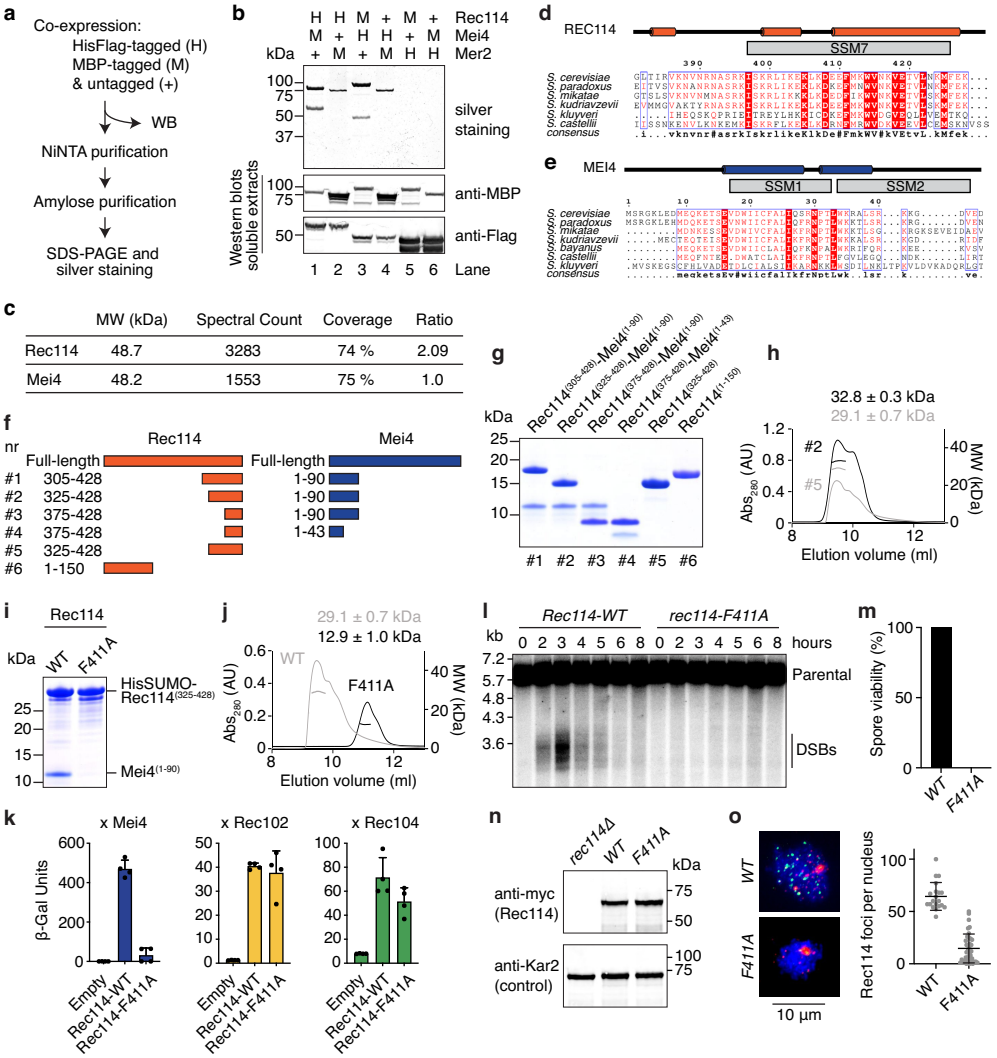

Extended Data Fig. 1 | Characterization of the Rec114–Mei4 complex. **a**, Strategy for purification of a hypothetical Rec114–Mei4–Mer2 (RMM) complex. Combinations of MBP-tagged and HisFlag-tagged RMM subunits were co-expressed in insect cells. After cell lysis, complexes were purified by sequential affinity chromatography and analysed by SDS–PAGE. Expression and solubility of the recombinant proteins were verified by western blotting (WB) of cell extracts. **b**, Analysis of purified complexes. Rec114–Mei4 complexes were apparent (lanes 1 and 3), but no Mer2 was co-purified. Lanes 2 and 4 show some enrichment of MBP–Mer2, but no co-purification of Rec114–Mei4. The presence of MBP–Mer2 in lanes 2 and 4 of the silver-stained gel may be due to background binding of MBP–Mer2 to the NiNTA resin (potentially via adsorption of DNA to the resin), or to low-affinity interactions with immobilized His-tagged Rec114–Mei4 complexes. Either way, none of the combinations tested yielded stoichiometric complexes of all three RMM subunits. Western blot controls of cell extracts showed that the tagged RMM proteins were expressed and soluble. **c**, Mass spectrometry analysis of Rec114–Mei4 complexes. Purified Rec114–Mei4 complexes were treated with trypsin and analysed by LC–MS/MS. The ratio of spectral counts between Rec114 and Mei4 provides additional evidence supporting the 2:1 stoichiometry of the complex. **d**, **e**, Alignments and predicted secondary structures of the C terminus of Rec114 (**d**) and the N terminus of Mei4 (**e**). The positions of the conserved SSMs are indicated. **f**, Cartoon of the Rec114–Mei4 truncations analysed. **g**, Purification of Rec114–Mei4 truncations. Proteins were expressed in *E. coli* and purified on NiNTA resin using a HisSUMO tag fused to the N terminus of the Rec114 fragment. After removal of the tag by treatment with the SUMO protease Ulp1, complexes were further purified by gel filtration. A Coomassie-stained SDS–PAGE analysis of purified complexes is shown (5 μg was loaded for each sample). Polypeptides containing Rec114(375–428) and Mei4(1–43) retained the ability to interact (combination #4). **h**, SEC–MALS analysis of Rec114–Mei4 truncations. The data are consistent with expectations for truncations that contain two Rec114 subunits and one Mei4 subunit. The C terminus of Rec114 alone forms a dimer. **i**, Wild-type and F411A-containing variants of HisSUMO–Rec114(325–428) were co-expressed with Mei4(1–90) and purified by chromatography on NiNTA resin. The absence of the Mei4 fragment with Rec114(F411A) shows that the mutation abolishes the interaction with Mei4. **j**, SEC–MALS analysis of untagged wild-type (WT, reproduced from **h** to aid comparison) and F411A mutant Rec114(325–428) shows that the mutation affects Rec114 dimerization. **k**, Y2H analysis of the interaction of Gal4BD–Rec114 (wild-type and F411A) with LexA–Mei4, LexA–Rec102, or LexA–Rec104 (mean + s.d. from four replicates). β-Gal units are quantified by hydrolysis of ONPG. The F411A mutation abolishes the interaction of Rec114 with Mei4, but not with Rec102 or Rec104. **l**, Southern blot analysis of meiotic DSB formation at the *CCT6* hotspot, showing that the *rec114*^{F411A} strain is defective in meiotic DSB formation. **m**, Spore viability of *rec114*^{F411A} mutant (n = 40). **n**, Western blot analyses of meiotic protein extracts from myc-tagged wild-type and *rec114*^{F411A} strains. The F411A mutation does not compromise the expression of Rec114. **o**, Left, immunofluorescence microscopy analysis of meiotic chromosome spreads with wild-type and F411A myc-tagged Rec114. Green, anti-myc; red, synaptonemal complex component Zip1; blue, DNA. Right, number of Rec114 foci per leptotene or early zygotene cell; mean ± s.d. (n = 20 and 38 cells for wild-type and F411A, respectively). The F411A mutation abolishes the formation of chromatin-associated Rec114 foci.

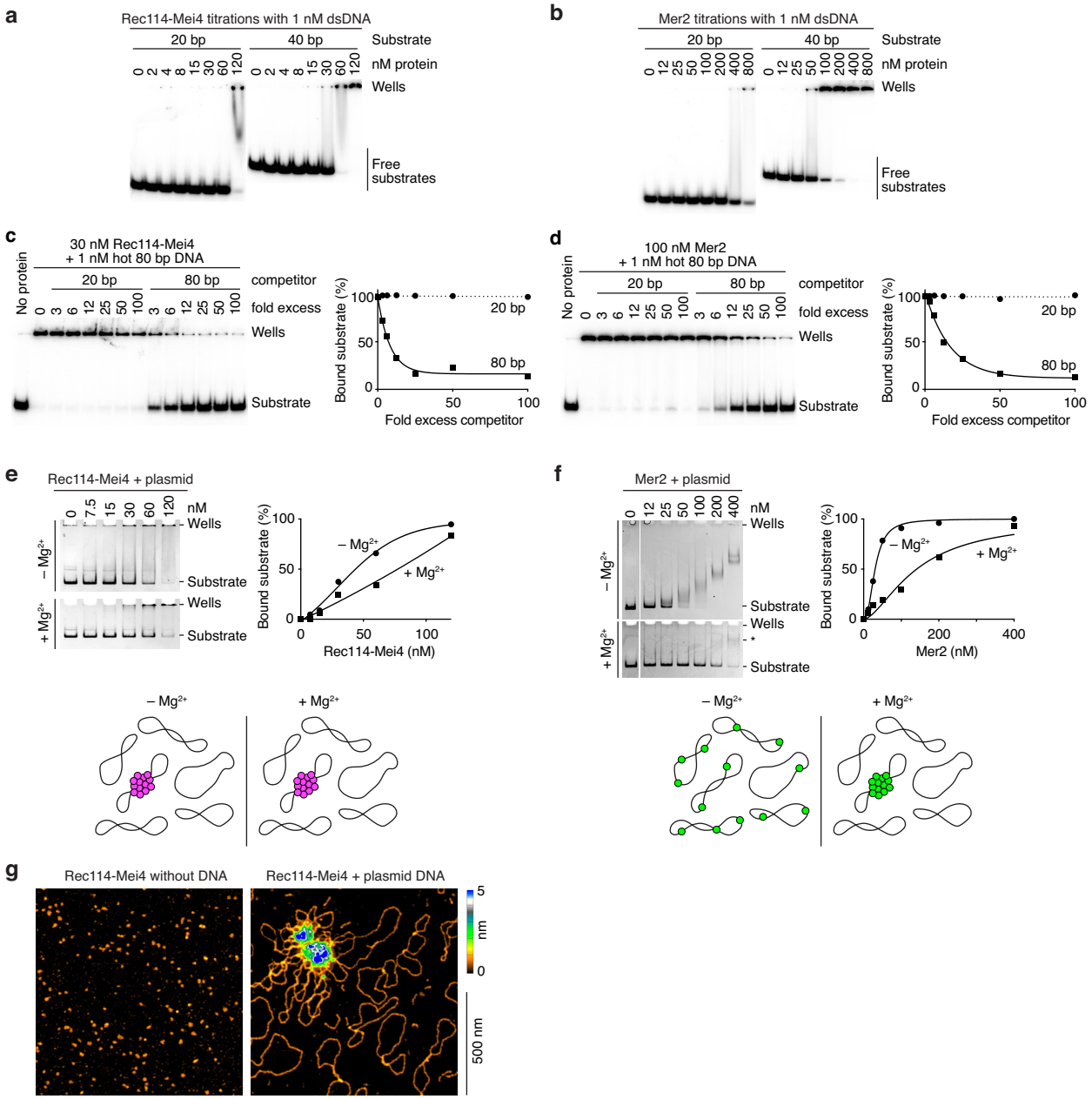

Extended Data Fig. 2 | DNA-binding properties of Rec114–Mei4 and Mer2 complexes. a, **b**, Gel shift analysis of binding of Rec114–Mei4 (**a**) and Mer2 (**b**) to 20- or 40-bp DNA substrates. Quantification is in Fig. 2b. **c**, **d**, Competition assay of Rec114–Mei4 (**c**) or Mer2 (**d**) binding to 80 bp radiolabelled DNA (1 nM) in the presence of 20 or 80 bp cold competitor. Fold excess is in nucleotides. Lines are one-phase decay fits. **e**, **f**, Binding to plasmid DNA analysed by native agarose gel electrophoresis. Rec114–Mei4 (**e**) and Mer2 (**f**) were titrated with 2 nM plasmid DNA (pUC19) in the presence or absence of 5 mM $MgCl_2$. Rec114–Mei4 complexes bound with roughly similar affinity independently of the presence of Mg^{2+} (apparent $K_D \approx 50–80$ nM). The apparent affinity is substantially lower than suggested by the gel shift analyses with radiolabelled substrates presented in **a** and Fig. 2a, b (apparent affinities in Fig. 2 legend). We suggest that this difference is because the proteins coalesce on a small fraction of the plasmid molecules, as illustrated in the cartoon below. Indeed, bound plasmids remained trapped in the wells, which is consistent with cooperative assembly of large nucleoprotein structures. Because each plasmid substrate provides many more binding sites than the short oligo substrates in **a** and Fig. 2a, a higher concentration of protein is required to reach complete binding of all of the plasmid molecules. In contrast to Rec114–Mei4, Mer2 showed efficient binding in the absence of Mg^{2+} in this assay ($K_D = 30 \pm 2$ nM) but binding appeared to be considerably inhibited in the presence of Mg^{2+} ($K_D \approx 150$ nM), as indicated by the persistence of unbound substrate at high protein concentrations. However, although the electrophoretic mobility of Mer2-bound plasmids decreased steadily as the concentration of Mer2 increased in the absence of Mg^{2+}, no such steady progression was observed when Mg^{2+} was included. Instead, a minority of bound substrates shifted to a low-mobility species (* in **f**), indicating that they were occupied by multiple Mer2 complexes. We interpret this as that, rather than inhibiting DNA binding, Mg^{2+} promotes cooperativity, in agreement with the fluorescence microscopy analysis (Extended Data Fig. 3b). The difference in migration distance of the plasmid between the gels with and without Mg^{2+} is due to the presence of Mg^{2+} in the electrophoresis buffer. **g**, AFM imaging of 12 nM Rec114–Mei4 in the absence (left) or presence (right) of 1 nM plasmid DNA (pUC19).

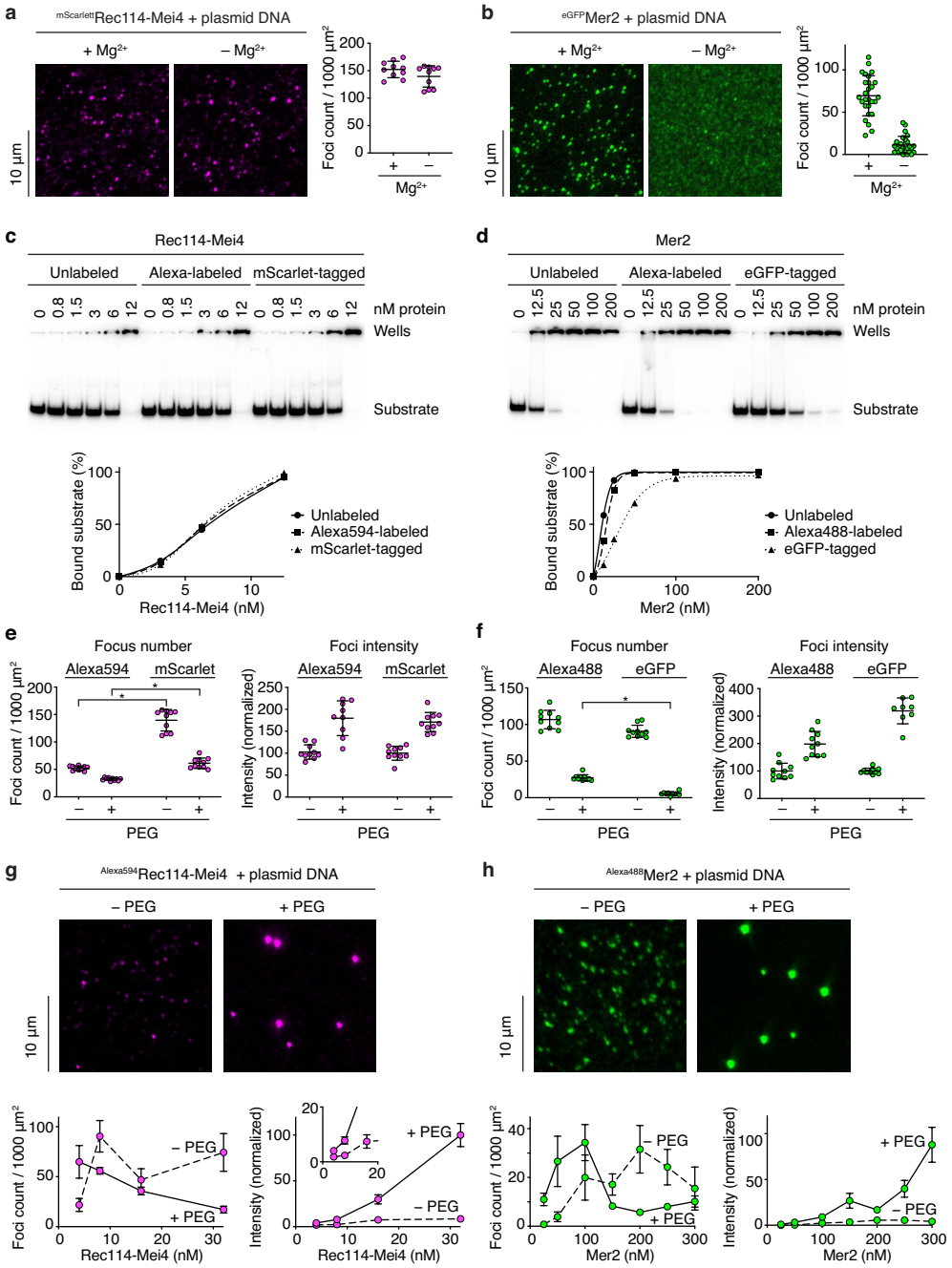

Extended Data Fig. 3 | See next page for caption.

Extended Data Fig. 3 | Properties of Rec114–Mei4 and Mer2 DNA-dependent condensates. a, **b**, Visualization of nucleoprotein condensates by epifluorescence microscopy using tagged Rec114–Mei4 (**a**) or Mer2 (**b**) in the presence or absence of 5 mM $MgCl_2$. Foci were defined using a fixed intensity threshold between samples. Each point represents the measurement from a field of view. Mean ± s.d. from 10 fields of view of 1.7×10^4 μm^2 (**a**) or 27 and 26 sections of 400 μm^2 with and without Mg^{2+}, respectively (**b**). **c**–**f**, Effect of fluorophore labelling or tagging on the DNA-binding and DNA-driven condensation activities of Rec114–Mei4 and Mer2 complexes. Labelling with Alexa594 or Alexa488 was achieved using amine-reactive fluorophores. Tagging was achieved by fusion of Rec114 with the monomeric fluorescent protein mScarlet or fusion of Mer2 with the weakly dimerizing fluorescent protein eGFP. The results described here indicate that covalent Alexa labelling has little, if any, effect on the DNA binding properties of these complexes, whereas fluorescent protein tagging caused subtle alterations in DNA binding and/or condensation. In most subsequent experiments, we used the dye-labelled complexes to minimize steric effects or oligomerization of fluorescent protein tags. **c**, Gel-shift analysis of binding of unlabelled, Alexa594-labelled, or mScarlet-tagged Rec114–Mei4 complexes to an 80-bp radiolabelled DNA substrate. The three versions of the Rec114–Mei4 complex have the same intrinsic DNA-binding activity. **d**, Gel-shift analysis of binding of unlabelled, Alexa488-labelled, or eGFP-tagged Mer2 complexes to an 80-bp radiolabelled DNA substrate. The DNA-binding activity of the Alexa-labelled Mer2 complex is nearly identical to the untagged protein, but the eGFP-tagged complex has 3.5-fold reduced DNA-binding activity. **e**, A comparison between Alexa-labelled and mScarlet-tagged Rec114–Mei4 complexes for DNA-driven condensation. Focus numbers (left) and total fluorescence intensity within foci normalized to the no-PEG samples (right) are shown for the complexes in the presence or absence of 5% PEG. With and without PEG, mScarlet-tagged Rec114–Mei4 produced more foci than the Alexa-labelled version. Because intrinsic DNA binding was indistinguishable between the complexes (**c**), we infer that the mScarlet-tagged complexes had a reduced efficiency in the cooperative formation of large condensates compared to the Alexa-labelled version, producing more numerous foci. *$P < 0.0001$ (two-tailed *t*-test). Mean ± s.d. from 8–10 fields of view. **f**, As in **e**, for comparison between Alexa-labelled and eGFP-tagged Mer2 complexes for DNA-driven condensation. The two labelled complexes show different numbers and intensities of foci in the presence of PEG. It is likely that the DNA-binding defect of the eGFP construct (**d**) leads to the formation of fewer, brighter condensates. It is possible that the weak dimerization activity of eGFP also contributes. *$P < 0.0001$ (two-tailed *t*-test). Mean ± s.d. from 9–10 fields of view. **g**, **h**, Top, effect of a crowding agent (PEG) on formation of nucleoprotein condensates visualized using covalently fluorophore-labelled Rec114–Mei4 (**g**) or Mer2 (**h**). Bottom, effect of protein concentration on DNA-driven condensation in the presence or absence of 5% PEG. Left, focus numbers; right, total fluorescence intensity within foci (normalized to the mean of the highest intensity sample). Mean ± s.d. from 4–6 fields of view (**g**) or 7–10 fields of view (**h**). The titrations reveal complex behaviours. **g**, In the presence of PEG, titration of Rec114–Mei4 from 4 to 32 nM led to a steady decrease in the number of foci, which was accompanied by a concomitant increase in focus intensity. In the absence of PEG, however, the number of Rec114–Mei4 foci first peaked at 8 nM before decreasing as the intensity of the foci started to increase. Nevertheless, focus intensity plateaued at a much lower intensity than in the presence of PEG. **h**, In the case of Mer2, titration from 25 to 300 nM in the presence of PEG yielded a peak in the number of foci at about 100 nM, which then sharply declined and stabilized beyond 150 nM. Consistently, Mer2 foci remained at a constant, low intensity between 25 and 100 nM, then became abruptly brighter above 100 nM. In the absence of PEG, the number of Mer2 foci increased between 25 and 200 nM, then started to decrease beyond that threshold. These behaviours are likely to reflect the complex combined effects of nucleation, growth, and collapse of the condensates, each of which is each affected differently by protein concentrations and by the crowding effect provided by PEG. See Source Data for exact *n* values for **e**–**h**.

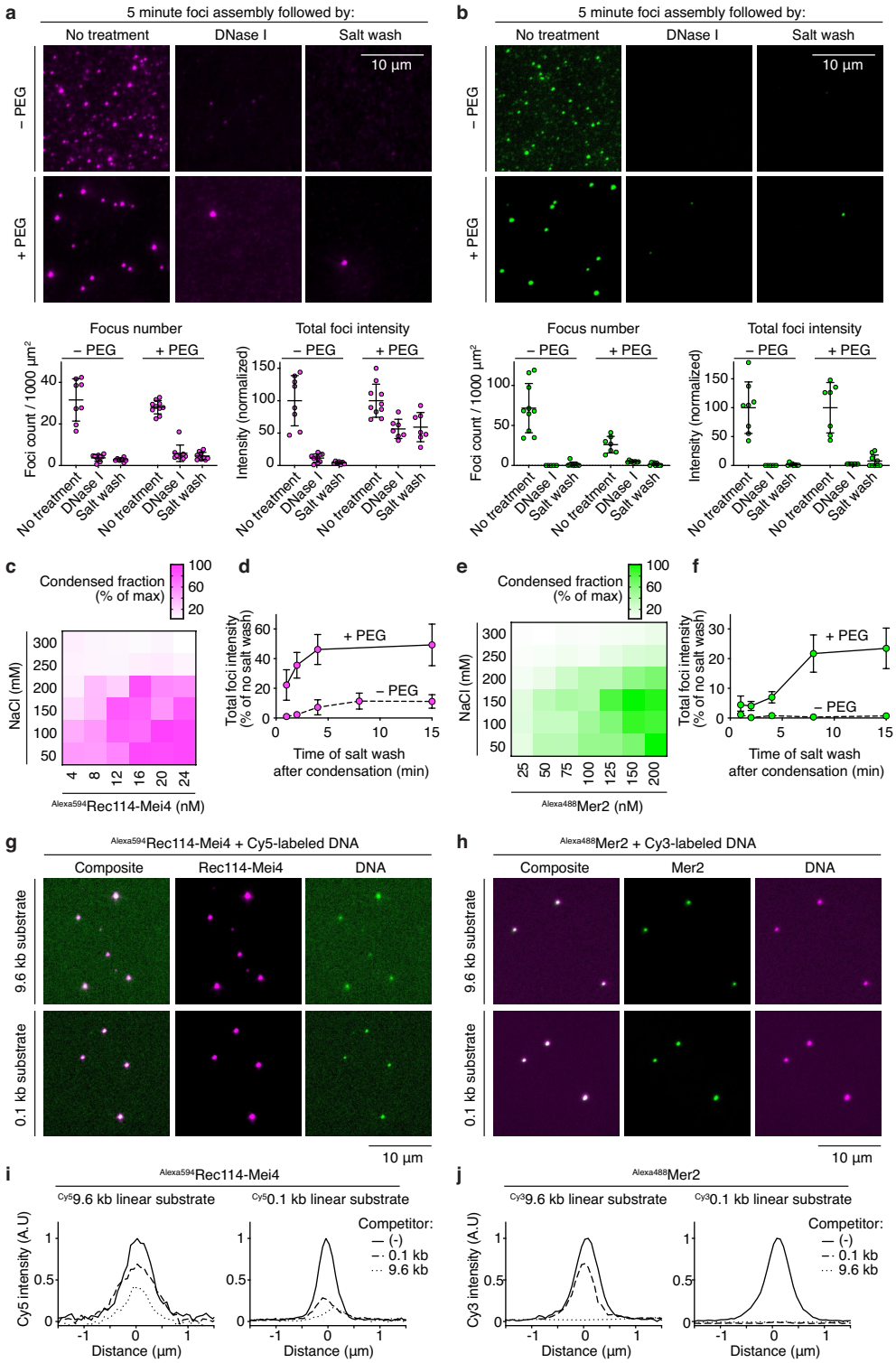

Extended Data Fig. 4 | See next page for caption.

Extended Data Fig. 4 | Properties of Rec114–Mei4 and Mer2 DNA-dependent condensates. a, **b**, Effect of challenging Rec114–Mei4 (**a**) or Mer2 (**b**) nucleoprotein condensates with DNase I or 0.5 M NaCl. Condensates were assembled for 5 min before challenge. Bottom, quantification of focus numbers per 1,000 μm^2 and of the total fluorescence intensity within foci within fields of view (normalized to mean of the no-treatment controls). Mean ± s.d. from 5–10 fields of view. **c**, **e**, Titrations of Rec114–Mei4 (**c**) and Mer2 (**e**) in the presence of DNA and PEG and various concentrations of NaCl. Heat maps represent the fraction of fluorescence signal found within foci. Condensed fractions are maximal at high protein and low salt concentrations. At all protein concentrations, condensation is essentially abolished beyond 250 mM NaCl. This suggests that electrostatic interactions, probably between the negatively charged DNA backbone and positively charged protein residues, are important for condensation. **d**, **f**, Time dependence for irreversibility of Rec114–Mei4 (**d**) and Mer2 (**f**) condensates. Some phase-separated liquid droplets have been shown to mature over time and progressively adopt gel-like or solid states[35,37–39]. Such sol–gel transitions may occur spontaneously through different mechanisms, including fibrillization and entanglement, and are thought to be counteracted in vivo to prevent the progressive accumulation of amyloid-like structures associated with pathological states[35]. To address whether our condensates are prone to progressive hardening, we queried the effect of assembly time on reversibility. We performed a time-course experiment in which the condensates were challenged by treatment with 0.5 M NaCl after an indicated period of assembly in the presence or absence of PEG. The graphs show the total intensity summed for foci within fields of view, expressed as a percentage of the intensity without a salt challenge. Mean ± s.d. for 6–10 fields of view. With Rec114–Mei4, 10% and 50% of fluorescent signal became refractory to the salt wash within 5 min of incubation time in the absence and presence of PEG, respectively (see **a** for example images and quantification). With Mer2, there was no evidence for the formation of irreversible structures in the absence of PEG during the course of the experiment. However, up to 25% of the focus intensity resisted the salt wash treatment after 8 min of incubation time in the presence of PEG. Therefore, both Rec114–Mei4 and Mer2 have a propensity to form more stable, perhaps gel-like, structures over time. Under our experimental conditions, this was more evident for Rec114–Mei4 than for Mer2, and was accentuated by molecular crowding. **g**, **h**, Assembly of Rec114–Mei4 (**g**) and Mer2 (**h**) with fluorescently labelled 9.6-kb and 100-bp linear DNA substrates. The overlap between the protein foci and puncta of DNA shows that the DNA is also enriched in the condensates. However, in contrast to the protein signal, the fluorescent signal of the DNA covers the slide because DNA is in excess and does not condense by itself. **i**, **j**, Competition between long and short DNA substrates for incorporation into condensates. Rec114–Mei4 (**i**) or Mer2 (**j**) condensates were assembled in the presence of a fluorescently labelled DNA substrate with or without 20-fold nucleotide excess of unlabelled competitor. The amount of fluorescent DNA signal averaged between ten foci is plotted. In each case, the 9.6-kb substrate was a more effective competitor than the 100-bp substrate. In addition, the 100-bp substrate was more successful at competing with the 100-bp fluorescent substrate than with the 9.6-kb fluorescent substrate. This preference for large DNA substrates is consistent with the hypothesis that the condensates form through multivalent interactions between the positively charged residues of Rec114–Mei4 or Mer2 and the sugar-phosphate backbone of the DNA. See Source Data for exact *n* values for **a**, **b**, **d**, **f**.

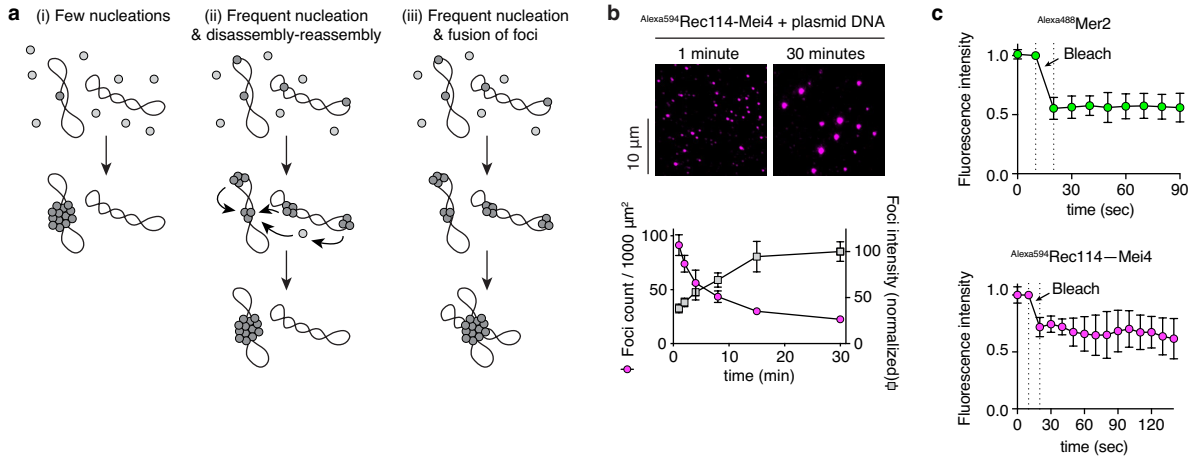

Extended Data Fig. 5 | Growth of DNA-driven condensates by fusion. **a**, Three scenarios for the assembly of DNA-driven condensates. (i) Nucleation could be limiting, with focus growth resulting principally from incorporation of protein from soluble pools. (ii) Frequent nucleation events could occur, initially leading to large numbers of small foci, whereupon some foci dissolve and others grow. (iii) Frequent nucleation could yield numerous small foci that then collide and fuse to yield fewer, larger foci. See Supplementary Discussion 2 for more detail. **b**, Time course of the assembly of Rec114–Mei4 foci in the presence of plasmid DNA. The *x*-axis indicates the time in solution before plating, upon which DNA is immobilized to the glass slide while soluble protein is still free to diffuse. Plot shows focus numbers and average focus intensity (normalized to the mean at 30 min). Mean ± s.d. from ten fields of view. **c**, FRAP experiments with Mer2 and Rec114–Mei4 condensates. Mean ± s.d. for six photobleached condensates.

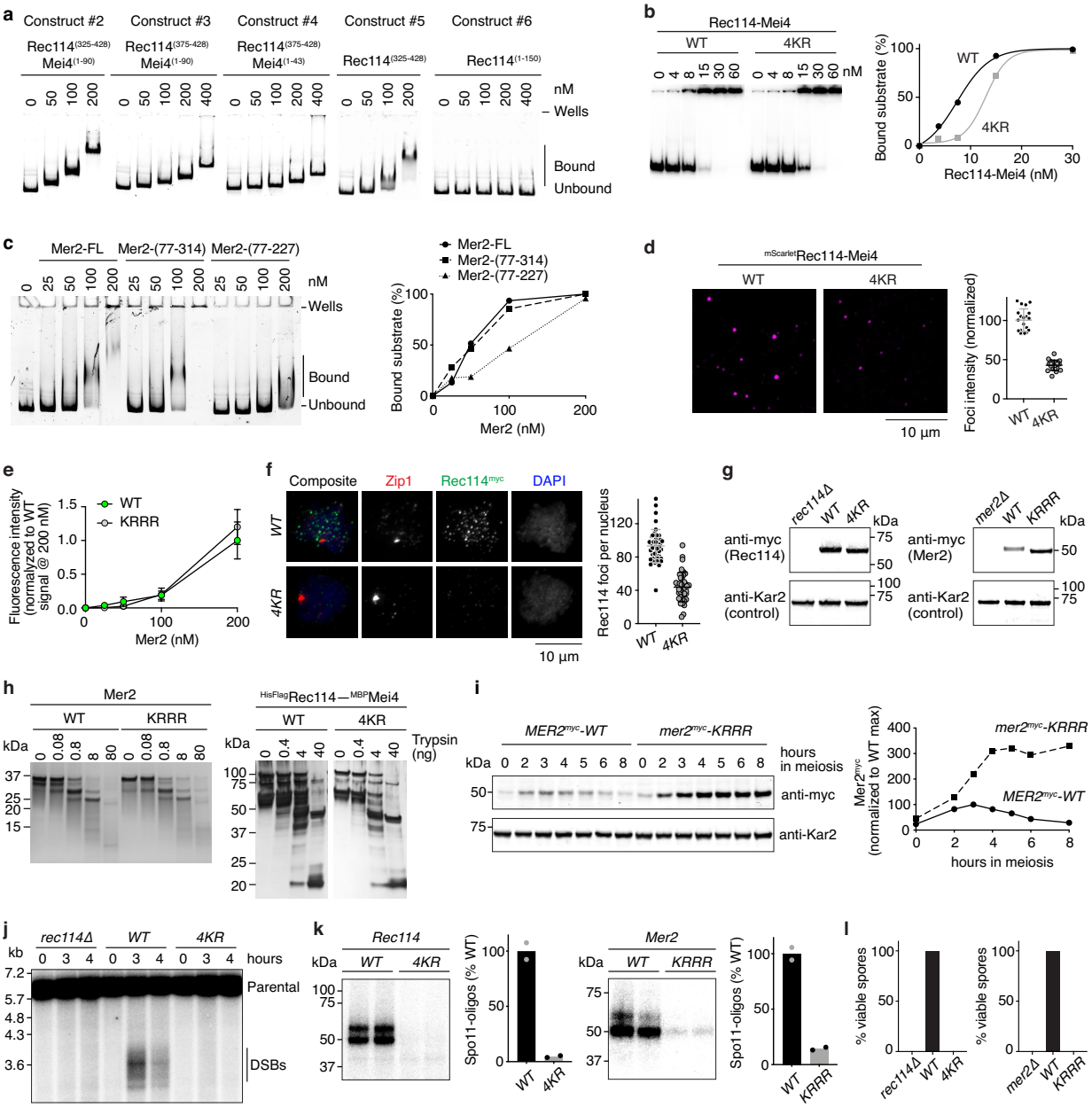

Extended Data Fig. 6 | See next page for caption.

Extended Data Fig. 6 | Identification of DNA-binding residues and effect of DNA binding on condensation in vitro and in vivo and on Spo11-induced break formation. a, Mapping the DNA-binding domain of Rec114–Mei4 complexes. Gel-shift analysis was performed with pUC19 plasmid DNA and the Rec114–Mei4 protein constructs shown in Extended Data Fig. 1f. Constructs #2, #3 and #4, which include the C terminus of Rec114 and the N terminus of Mei4, were competent for DNA binding. The difference in mobility of shifted species between these constructs is in line with the difference in sizes of the protein complexes. Mei4 is dispensable for DNA binding by Rec114 (construct #5 lacks Mei4). The N terminus of Rec114 alone, encompassing the PH domain, did not bind DNA (construct #6). None of the constructs showed evidence for cooperative DNA binding (unlike the full-length protein (Extended Data Fig. 2e)), suggesting that they do not undergo DNA-driven condensation. **b**, Gel shift analysis of wild-type and mutant Rec114–Mei4 complexes binding to an 80-bp DNA substrate. The Rec114(4KR) mutant has residues R395, K396, K399, and R400 mutated to alanine. Lines on graphs are sigmoidal curve fits. **c**, Mapping the DNA-binding domain of Mer2. Gel-shift analysis was performed with pUC19 plasmid DNA and HisSUMO-tagged Mer2 protein that was full-length (FL), had the N terminus removed (fragment 77–314), or had both the N and C termini removed (fragment 77–227). Deleting the N terminus alone had no significant effect on DNA binding, but further deleting the C terminus strongly reduced DNA binding. **d**, Effect of the Rec114(4KR) mutation on condensation in vitro. Reactions included 5% PEG. Each point is the average of the intensities of foci in a field of view ($n = 20$ fields), normalized to the overall mean for wild type. Mean ± s.d. **e**, Incorporation of Mer2(KRRR) into preformed condensates. Condensates were assembled with 100 nM unlabelled Mer2. Reactions were then supplemented with the indicated amount eGFP–Mer2 (wild-type or KRRR) and plated immediately. Incorporation of eGFP-tagged complexes within condensates was quantified. Mean ± s.d. from 20 fields of view. **f**, Immunofluorescence on meiotic chromosome spreads for myc-tagged Rec114. The number of foci per leptotene or early zygotene cell is plotted. Mean ± s.d. ($n = 44$ and 40 cells for wild-type and *rec114*^{4KR} strains, respectively). **g**, Immunoblotting of meiotic protein extracts for wild-type and mutant Rec114 (left) or Mer2 (right). **h**, Partial proteolysis of wild-type and mutant Mer2 and Rec114–Mei4 complexes. **i**, Immunoblot analysis of wild-type Mer2 and Mer2(KRRR). Protein extracts of meiotic time courses were analysed by SDS–PAGE followed by immunoblotting against Mer2–myc. Anti-Kar2 was used as a loading control. Quantification of immunoblot signal is plotted. Mer2(KRRR)–myc reached higher steady-state protein levels and persisted longer than wild-type Mer2–myc. A previous study showed that mutating an essential CDK phosphorylation site of Mer2 (Ser30) or inhibiting CDK activity led to reduced turnover of Mer2, similar to the effect of the KRRR mutant[15]. This is consistent with the hypothesis that Mer2 turnover is tied to phosphorylation, which requires DNA binding. **j**, Southern blot analysis of meiotic DSB formation at the *CCT6* hotspot in strains expressing wild-type or mutant Rec114 protein. **k**, Labelling of Spo11–oligo complexes in wild-type and mutant Rec114 (left) and Mer2 (right) strains. Points represent two biological replicates. **l**, Spore viability of strains expressing wild-type or mutant Rec114 (left) and Mer2 (right) ($n = 40$). For gel source data, see Supplementary Fig. 1.

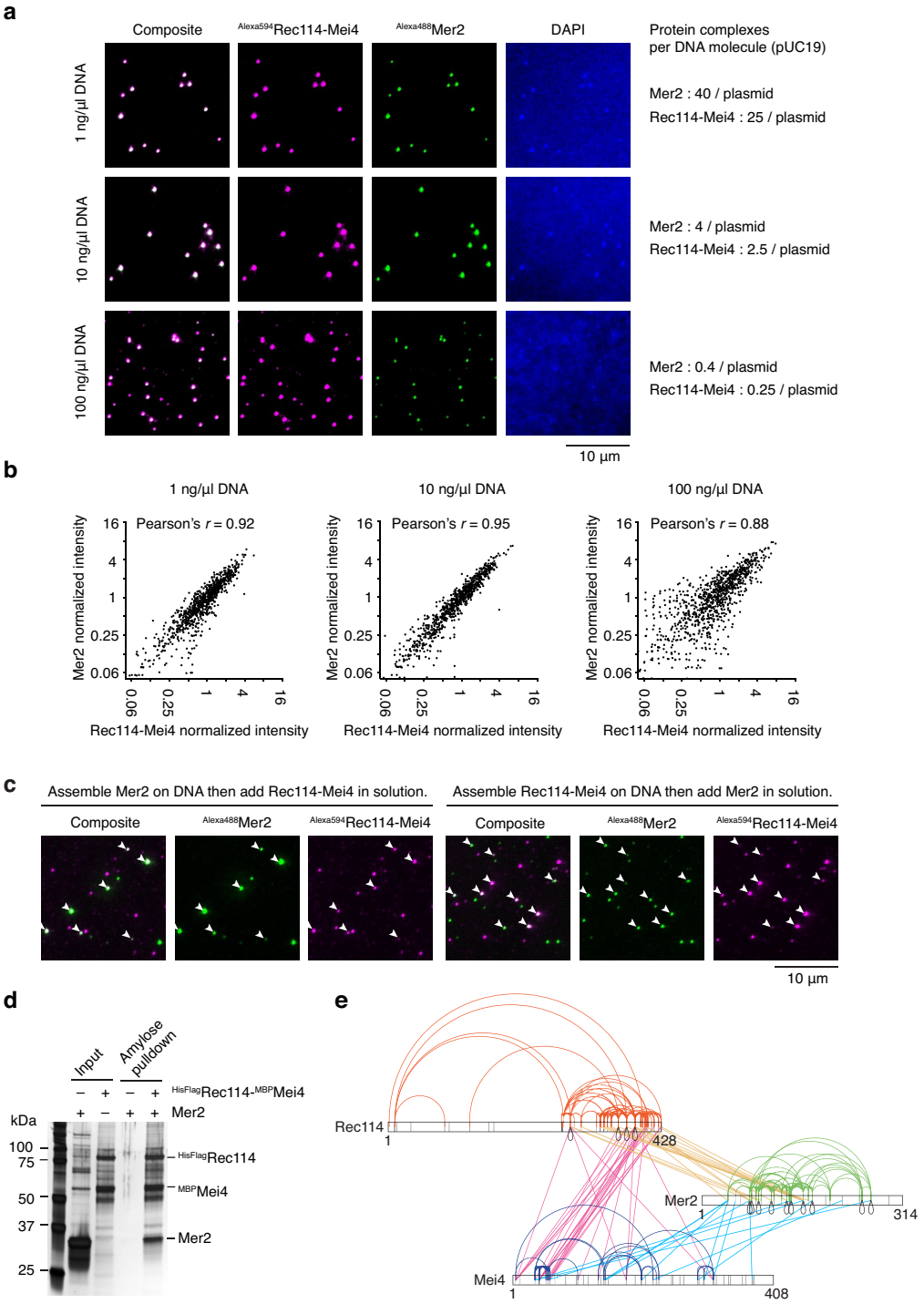

Extended Data Fig. 7 | Rec114–Mei4 and Mer2 form mixed condensates. **a**, Rec114–Mei4 colocalizes with Mer2 in mixed condensates irrespective of DNA concentration. Reactions containing 16 nM Rec114–Mei4 and 100 nM Mer2 in the presence of 1, 10, or 100 ng µl^{-1} plasmid DNA were assembled for 20 min at 30 °C. DAPI (5 µg ml^{-1}) was added to the reaction before application to glass slides. DNA enrichment within the condensates is visible at lower DNA concentrations (top, middle), but is not as clear at high DNA concentrations (bottom). The ratios of Rec114–Mei4 (heterotrimers) and Mer2 (tetramers) to each 2.6-kb plasmid DNA molecule are indicated on the right. Colocalization of Rec114–Mei4 and Mer2 complexes is evident even with a molar excess of DNA molecules, demonstrating that formation of joint foci is not simply because both protein complexes are independently associating with a limiting number of DNA substrates. **b**, Correlated intensity of Rec114–Mei4 and Mer2 proteins within the condensates. Each point shows the fluorescence intensity in an individual focus (n = 950, 925 and 1,000 foci from 2–3 fields of view for samples with 1, 10 and 100 ng µl^{-1} DNA, respectively), normalized to the average focus intensity per field of view. The strong correlation indicates that the composition of the condensates is highly uniform between foci. In the presence of high DNA concentration, the fraction of smaller foci increased and correlated intensities decreased. **c**, Recruitment of soluble Rec114–Mei4 (left) or Mer2 (right) into preassembled condensates of Mer2 (left) or Rec114–Mei4 (right). Arrowheads, examples of the preassembled condensates. **d**, Pulldown of purified Mer2 on amylose resin with or without immobilized Rec114–Mei4 complexes. **e**, XL–MS of Rec114–Mei4–Mer2 condensates (620 crosslinked peptides, 229 distinct crosslinked pairs of lysines).

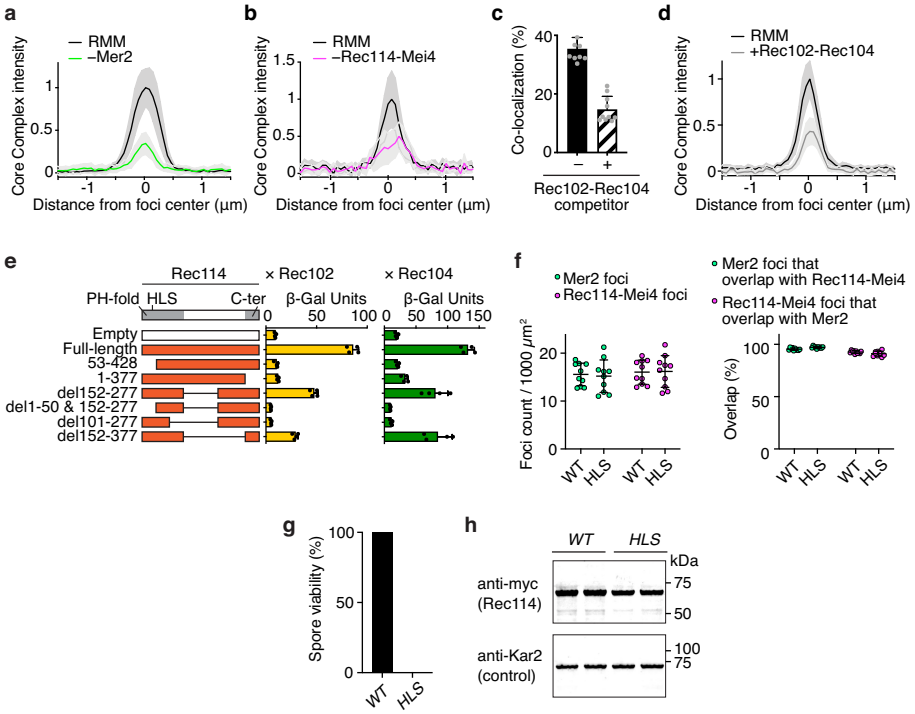

Extended Data Fig. 8 | Recruitment of the Spo11 core complex to Rec114–Mei4–Mer2 condensates. a, Quantification of core complex signal within Rec114–Mei4 foci in the presence (100 nM) or absence of Mer2. The average intensity within 20 foci is plotted for each reaction. Shaded areas represent 95% confidence intervals (CI). **b**, Quantification of core complex signal within Mer2 foci in the presence (16 nM) or absence of Rec114–Mei4. Reactions contained 25 nM Mer2. The average intensity within 20 foci is plotted for each reaction. Shaded areas represent 95% CI. **c**, Effect of including 100 nM MBP–Rec102–Rec104–HisFlag competitor on the recruitment of the core complex to RMM condensates (16 nM Rec114–Mei4, 100 nM Mer2). The fraction of Rec114–Mei4–Mer2 foci that contain detectable core complex signal is plotted (mean + s.d. from ten fields of view). **d**, Intensity of core complex signal within Rec114–Mei4–Mer2 condensates in the absence or presence of Rec102–Rec104 competitor. The average core complex intensity within 20 foci is plotted for each reaction. Shaded areas represent 95% CI. **e**, Mapping regions of Rec114 required for interaction with Rec102 or Rec104 by Y2H analysis. β-Galactosidase units are measured for the interaction between truncated variants of Gal4AD–Rec114 and LexA–Rec102 or LexA–Rec104 (mean + s.d. from four replicates). The position of the HLS mutation within the Rec114 PH-fold is indicated. **f**, Effect of the HLS mutation on the formation of comingled RMM condensates. Mean ± s.d. from ten fields of view. **g**, Spore viability of wild-type and *rec114*^{HLS} mutant strains. **h**, Immunoblot analysis of meiotic protein extracts from myc-tagged wild-type and *rec114*^{HLS} mutant strains. Samples from two biological replicates are shown. For gel source data, see Supplementary Fig. 1.

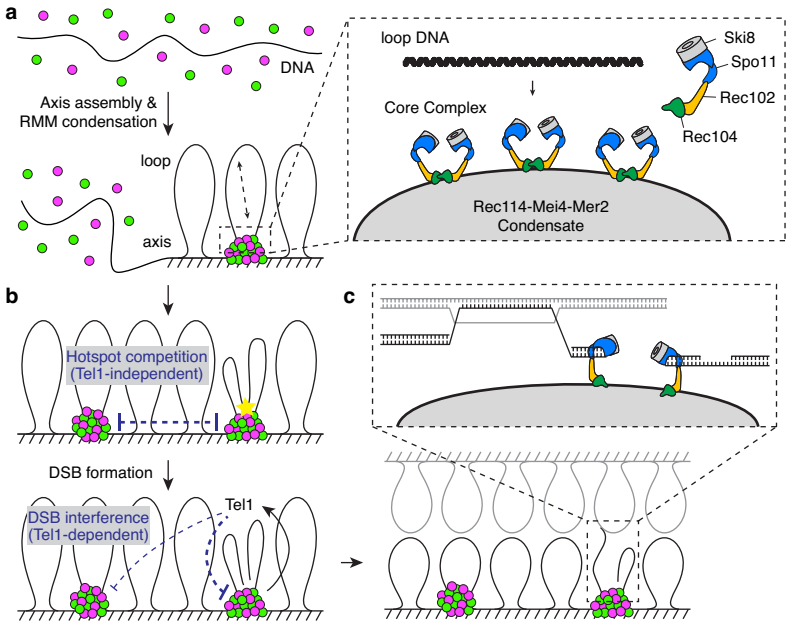

Extended Data Fig. 9 | A condensate model for assembly of the meiotic DSB machinery and implications for the control of DSB formation and repair. **a**, Assembly of the DSB machinery. Left, Rec114–Mei4 and Mer2 complexes bind DNA in a highly cooperative manner to form large mixed nucleoprotein condensates. Right, these condensates provide a platform to recruit the core complex through interactions that involve the N-terminal domain of Rec114 and the Rec102–Rec104 components of the core complex. Multiple Spo11 complexes are recruited and may engage an incoming DNA loop simultaneously. The molecular arrangement of the core complex proteins is based on ref. [10]. See Supplementary Discussion 4 for more detail. **b**, Hotspot competition and DSB interference. Competition arises before DSB formation as a consequence of the partitioning of RMM proteins into condensates. DSB interference is implemented through local inhibition of further DSB formation by DSB-activated Tel1. Inhibition could work on the same cluster that generated the activation DSB as well as on nearby clusters *in cis*. See Supplementary Discussion 5 for more detail. **c**, The coherence provided by the condensates may serve functions during repair, including the maintenance of a physical connection between the DNA ends that involves end-capping by condensate-embedded core complexes. See Supplementary Discussion 6 for more detail.

nature research

Corresponding author(s): Scott Keeney and Corentin Claeys Bouuaert

Last updated by author(s): Feb 7, 2021

Reporting Summary

Nature Research wishes to improve the reproducibility of the work that we publish. This form provides structure for consistency and transparency in reporting. For further information on Nature Research policies, see our Editorial Policies and the Editorial Policy Checklist.

Statistics

For all statistical analyses, confirm that the following items are present in the figure legend, table legend, main text, or Methods section.

n/a	Confirmed
☐	☒ The exact sample size (*n*) for each experimental group/condition, given as a discrete number and unit of measurement
☐	☒ A statement on whether measurements were taken from distinct samples or whether the same sample was measured repeatedly
☐	☒ The statistical test(s) used AND whether they are one- or two-sided *Only common tests should be described solely by name; describe more complex techniques in the Methods section.*
☒	☐ A description of all covariates tested
☐	☒ A description of any assumptions or corrections, such as tests of normality and adjustment for multiple comparisons
☐	☒ A full description of the statistical parameters including central tendency (e.g. means) or other basic estimates (e.g. regression coefficient) AND variation (e.g. standard deviation) or associated estimates of uncertainty (e.g. confidence intervals)
☐	☒ For null hypothesis testing, the test statistic (e.g. *F*, *t*, *r*) with confidence intervals, effect sizes, degrees of freedom and *P* value noted *Give P values as exact values whenever suitable.*
☒	☐ For Bayesian analysis, information on the choice of priors and Markov chain Monte Carlo settings
☐	☒ For hierarchical and complex designs, identification of the appropriate level for tests and full reporting of outcomes
☐	☒ Estimates of effect sizes (e.g. Cohen's *d*, Pearson's *r*), indicating how they were calculated

Our web collection on statistics for biologists contains articles on many of the points above.

Software and code

Policy information about availability of computer code

Data collection	Microscopy data was acquired with Slidebook 7 (Intelligent Imaging Innovations) software. Protein chromatography data were collected using Unicorn 5 (GE Healthcare). SEC-MALS data collection used Chemstation software (B.04.03-SP1, Agilent Technologies, Wilmington, DE) and ASTRA V software (Wyatt Corp., Santa Barbara, CA).
Data analysis	Data analyses were conducted using GraphPad Prism (version 8). Microscopy data was analyzed in Image J 2.1.0 using a custom-made script described in Methods and available at https://github.com/claeysbouuaert/scripts. Crosslinking data was analyzed using pLink and maps generated with xiNET. Mass spectrometry analysis of Rec114-Mei4 were performed using Mascot (Matrix Science, version 2.6.100). Scaffold (version Scaffold_4.8.4, Proteome Software Inc., Portland, OR) was used to validate MS/MS based peptide and protein identifications. Protein probabilities were assigned by the Protein Prophet algorithm.

For manuscripts utilizing custom algorithms or software that are central to the research but not yet described in published literature, software must be made available to editors and reviewers. We strongly encourage code deposition in a community repository (e.g. GitHub). See the Nature Research guidelines for submitting code & software for further information.

Data

Policy information about availability of data

All manuscripts must include a data availability statement. This statement should provide the following information, where applicable:

- Accession codes, unique identifiers, or web links for publicly available datasets
- A list of figures that have associated raw data
- A description of any restrictions on data availability

Source data for gels, blots, and graphs for Figs. 1, 2, 3, 4, blots for ED Figs. 6, 8, and data for graphs in ED Figs. 3, 4 are available with the paper. Processed

crosslinking-mass spectrometry data are provided in Supplementary Table 1. Fasta sequences of the yeast SK1 strain are available at https://www.yeastgenome.org. Swissprot reviewed database is available at www.UniProt.org.

Field-specific reporting

Please select the one below that is the best fit for your research. If you are not sure, read the appropriate sections before making your selection.

☒ Life sciences ☐ Behavioural & social sciences ☐ Ecological, evolutionary & environmental sciences

For a reference copy of the document with all sections, see nature.com/documents/nr-reporting-summary-flat.pdf

Life sciences study design

All studies must disclose on these points even when the disclosure is negative.

Sample size	No sample size calculations were performed. Sample sizes were chosen based on established best practices in the field for experimental methods used.
Data exclusions	No samples were excluded, except for the analysis of condensates by microscopy where some outlier images were excluded if out of focus (blurry) or with signal too low to quantify accurately.
Replication	All conclusions described in the paper were based on findings reproduced in biological replicate experiments, except as specified in Statistics and Reproducibility section.
Randomization	Not relevant: All experiments involved comparison of isogenic control (wild type) and mutant yeast strains.
Blinding	Not relevant: All experiments involved comparison of isogenic control (wild type) and mutant yeast strains.

Reporting for specific materials, systems and methods

We require information from authors about some types of materials, experimental systems and methods used in many studies. Here, indicate whether each material, system or method listed is relevant to your study. If you are not sure if a list item applies to your research, read the appropriate section before selecting a response.

Materials & experimental systems

n/a	Involved in the study
☐	☒ Antibodies
☐	☒ Eukaryotic cell lines
☒	☐ Palaeontology and archaeology
☒	☐ Animals and other organisms
☒	☐ Human research participants
☒	☐ Clinical data
☒	☐ Dual use research of concern

Methods

n/a	Involved in the study
☒	☐ ChIP-seq
☒	☐ Flow cytometry
☒	☐ MRI-based neuroimaging

Antibodies

Antibodies used	anti-myc (9E10): Abcam (ab32) anti-Zip1: This laboratory anti-Kar2 (y-115): Santa Cruz (sc-33630) anti-Flag (M2): Sigma (F1804) HRP-conjugated anti-Flag (M2): Sigma (A8592) anti-MBP: NEB (E8032) goat anti-mouse IgG Alexa-488: Molecular Probes (A-11001) donkey anti-rabbit IgG Alexa-594: Molecular Probes (A-21207) IRDye 800CW goat anti-mouse IgG: Li-Cor (926-32210) IRDye 680 goat anti-rabbit IgG: Li-Cor (926-68071)
Validation	Except for anti-Zip1, these antibodies are standard reagents in molecular biology and their specificity for use in yeast is well established. Our study directly validates anti-Flag HRP and anti-MBP through differential electrophoretic mobility of fusion proteins in Extended Data Fig. 1b. In addition, absence of signal in the control in ED Fig. 1n, 6g validates the anti-myc antibody. The anti-Zip1 antibody was previously validated in studies of our laboratory showing absence of signal prior to meiotic entry (Henderson et al., 2006, DOI 10.1016/j.cell.2006.04.039). Validation data for anti-Flag (M2) is available at https://www.sigmaaldrich.com/content/dam/sigma-aldrich/docs/Sigma/General_Information/anti-flag-2poster.pdf and for anti-Kar2 (y-115) at https://datasheets.scbt.com/sc-33630.pdf.

Eukaryotic cell lines

Policy information about cell lines

Cell line source(s)	Sources of all yeast strains are given in Supplementary Table 4. Spodoptera frugiperda Sf9 cells for expression of recombinant proteins were from Gibco (Thermo Fisher 11496015).
Authentication	Yeast strains were verified by PCR and/or Southern blotting. Sf9 certificates of analyses are available at https://www.thermofisher.com/order/catalog/product/11496015#/11496015.
Mycoplasma contamination	Not applicable for yeast strains. Mycoplasma testing of Sf9 cells is referenced at https://www.thermofisher.com/order/catalog/product/11496015#/11496015
Commonly misidentified lines (See ICLAC register)	Not applicable (yeast strains and Sf9 cells only)